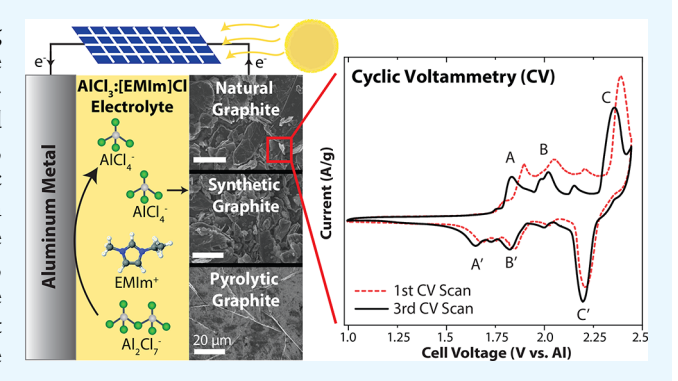
Effects of Graphite Structure and Ion Transport on the Electrochemical Properties of Rechargeable Aluminum—Graphite **Batteries**

Jeffrey H. Xu, Damon E. Turney, Ankur L. Jadhav, and Robert J. Messinger*

Department of Chemical Engineering, The City College of New York, CUNY, New York, New York 10031, United States

Supporting Information

ABSTRACT: Rechargeable aluminum—graphite batteries using chloroaluminate-containing ionic liquid electrolytes store charge when molecular chloroaluminate anions intercalate into graphite. However, the relationship between graphite structure and bulk electrochemical properties is not well understood. Here, we characterize the structure of natural, synthetic, and pyrolytic graphites and analyze their electrochemical performance in aluminum-graphite cells, revealing insights into their charge storage mechanisms, rate capabilities, Coulombic efficiencies, and extended cycling stabilities. Natural graphite exhibited the highest specific capacity at all potentials and the greatest capacity retention during variable-rate galvanostatic cycling. The compositions of the intercalated electrodes (C_x[AlCl₄]) were



determined coulometrically, and their stage numbers were rationalized by using a hard-sphere model. Variable-rate CV analyses establish that the rates of reversible electrochemical chloroaluminate intercalation in natural and synthetic graphites are effectively reaction-limited at potentials <2.1 V, and neither strongly diffusion- nor reaction-limited above 2.3 V, differing significantly from the diffusion-limited electrochemical intercalation of lithium cations into graphite. The results yield a new understanding of the relationships between graphite structure, ion transport, and electrochemical properties in rechargeable aluminum-graphite batteries and are expected to aid the rational design of graphite electrodes with enhanced electrochemical performance.

KEYWORDS: aluminum battery, graphite intercalation compound, ionic liquid, staging, ion transport

■ INTRODUCTION

Transformative advances in electrochemical energy storage are needed to electrify transportation and store intermittent renewable energy sources (e.g., solar and wind) on a global scale. Rechargeable lithium-ion batteries revolutionized portable electronics, but to store energy at larger scales, significant improvements are required in energy density, cycle life, cost, safety, and earth abundance. Nonincremental improvements are rooted in the development of new battery materials and chemistries. Aluminum (Al) metal exhibits a remarkable volumetric capacity (8.05 Ah/cm³, ~4 times greater than that of Li metal (2.06 Ah/cm³)) and gravimetric capacity (2.98 Ah/g, \sim 3/4 of Li metal (3.85 Ah/g)), where its high capacity is a result of three-electron electrochemical redox processes. Aluminum is also nonflammable, nontoxic, low cost, and the most abundant metal in the earth's crust.3 Despite great promise, scientific understanding and technological development of rechargeable aluminum metal batteries are still in their infancy.

In large part, Al battery development has been hindered by the lack of electrolytes that reversibly electroplate and electrostrip aluminum metal at room temperature as well as

the number of positive electrode materials that are chemically and electrochemically compatible with them.⁴⁻⁷ Much recent research on rechargeable aluminum batteries has used ionic liquid electrolytes containing AlCl₃ and a salt composed of an imidazolium cation with different alkyl side chains and a halide anion (e.g., Cl⁻), such as 1-ethyl-3-methylimidazolium chloride ([EMIm]Cl). Lewis acidic mixtures (molar ratio AlCl₃: [EMIm]Cl > 1.0), which contain the chloroaluminate anions AlCl₄ and Al₂Cl₇, enable Al metal to be reversibly electrodeposited at room temperature according to

$$4Al_2Cl_7^- + 3e^- \rightleftharpoons Al + 7AlCl_4^- \tag{1}$$

Graphite is an ideal electrode material due to its earth abundance, low cost, stability, high electrical conductivity, and the ability to intercalate various ions. Gifford et al.9 first demonstrated a prototype Al-graphite cell in 1988 using a molten salt electrolyte. Recently, in 2015, Lin et al. 10 and Sun et al. 11 demonstrated Al-graphite batteries using Lewis acidic

Received: June 14, 2019 Accepted: October 16, 2019 Published: October 16, 2019 mixtures of AlCl3:[EMIm]Cl electrolyte, which store charge when molecular chloroaluminate AlCl₄ anions electrochemically intercalate within the graphite electrodes. Since then, numerous research groups have reported Al-graphite batteries using different types of graphites.⁴⁻⁶ Depending on the graphite type, electrolyte, and cycling parameters, rechargeable Al-graphite cells exhibit discharge plateaus of ~2.2 and ~1.8 V, with discharge capacities up to 120 mAh/g at room temperature. Engineered graphites, such as graphitic foams and few/multilayered graphene-like materials, can enable ultrafast charge/discharge rates (>1–10's of A/g). 10,12–14

Despite these advances, the relationships between graphite structure and bulk electrochemical properties are still poorly understood. Various graphite-based electrodes have been investigated over the past few years, including pyrolytic, ^{10,15,16} synthetic, ¹⁷ and natural ^{12,18–21} graphite. Subsequent studies, which demonstrated improved rate capability and specific capacity by optimizing porosity, reducing ion-diffusion length scales, and enhancing electronic conductivity, include graphitic foams, ^{10,14,22} few-layered graphene, ²³ graphene aerogels, ^{24,25} and porous graphite/graphene-like ^{26–29} electrodes. For example, by using a high-temperature and high-pressure treatment process, Chen et al. 13 engineered a highly oriented graphenelike film cathode that retained a capacity of 120 mAh/g at 100 A/g after 250000 cycles. However, only a few in-depth direct comparisons have been made among different graphite structures, including the low-cost and minimally processed pristine graphites from which many advanced graphites are derived. For example, Mckerracher et al. 15 discussed the effects of porosity and crystallite size in the context of pyrolytic graphite and carbon paper electrodes, while Zhang et al.2 compared particle dimensions of graphite and few-layered graphene electrodes. To compare the effect of particle shape on electrochemical performance, Kravchyk et al.²¹ modified the shape of graphite flakes via ultrasonication or knife milling. Nonetheless, the "optimal" structure for battery performance is still elusive, particularly when considering the design of the graphite electrodes from the nanometer to macroscopic scales.

Here, we study how different graphite structures affect bulk electrochemical and ion transport properties in rechargeable aluminum-graphite batteries. Cells with aluminum metal negative electrodes, AlCl₃:[EMIm]Cl ionic liquid electrolytes, and natural, synthetic, and pyrolytic graphite positive electrodes were prepared and electrochemically characterized. Pristine graphites were characterized by X-ray diffraction (XRD), electron microscopy, X-ray photoelectron spectroscopy (XPS), and N₂ sorption measurements, revealing differences in their structures and defect concentrations. The cells were subjected to extended and variable-rate galvanostatic cycling as well as slow scan-rate (up from 20 μ V/s) and variable-rate cyclic voltammetry (CV). The effects of graphite structure are discussed on the charge storage mechanism, rate capabilities, Coulombic efficiency, and extended cycling stability. Intercalated compositions were determined coulometrically, while the theoretical capacity and graphite staging were analyzed with a hard-sphere model. Variable-rate CV measurements established quantitatively how ion mass transport affects reversible chloroaluminate intercalation as a function of potential and graphite type. Long-term galvanostatic cycling stabilities and improved cycling protocols were tested. Overall, this study yields insights into the relationships between graphite structure, ion transport, and electrochemical properties in Al-graphite cells.

■ EXPERIMENTAL SECTION

Composite Electrode Fabrication. Pyrolytic graphite foil (MTI, 99.90%) was used as received. Natural graphite flakes (Alfa Aesar, 99.995%) or KS44 synthetic graphite (TIMREX, 99.94%) was mixed with poly(vinylidene fluoride) (PVDF) binder (Sigma-Aldrich, average molecular weight 534000 g/mol) by using a mass ratio of 90:10 and dissolved in N-methyl-2-pyrrolidone (NMP) solvent (1 mL solvent/100 mg powder). The slurry was stirred for 10 min and agitated with a vortex mixer for 30 s and then cast on a molybdenum (Mo) foil current collector (20 μ m thick foil) by using a doctor-blade film coater (MTI). The electrode was vacuum-dried at 120 °C for 10 h to evaporate the NMP solvent. The final thickness and areal mass loading of the electrode material were $\sim 100 \ \mu m$ and 5 mg/cm², respectively. Electrode resistivity and conductivity were measured using a four-point probe. The electrode porosity was calculated by comparing the measured and theoretical density of graphite (Text S1, Supporting Information).

Cell Assembly. Polytetrafluorethylene (PTFE) Swagelok unions with 1/4 in. diameters (no. T-810-6) were used to fabricate airtight cells. The aluminum foil negative electrode (MTI, 99.99%, 0.1 mm thick), glass fiber separator (Whatman brand, GF/D), AlCl₃:[EMIm] Cl electrolyte (1.5:1 molar ratio, Iolitec, 30 μ L), and the graphite positive electrode were placed in the middle of the Swagelok union and compressed by Mo current collector rods (Figure 1). Battery

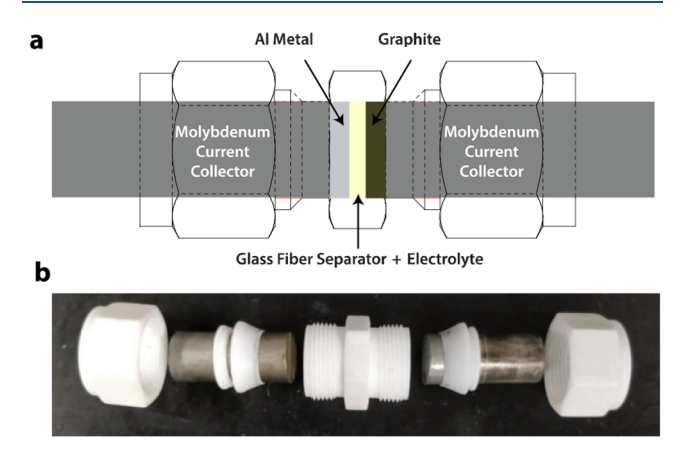


Figure 1. (a) Schematic of Swagelok-type cell assembly and components for Al-graphite battery. (b) Exploded view.

assembly was performed in an argon-filled glovebox (<1 ppm of H₂O and O₂). Excess electrolyte was used, and the total quantity of AlCl₄ anions in the electrolyte did not limit cell capacity.

Electrochemical Measurements. Galvanostatic cycling and cyclic voltammetry (CV) were performed with an Arbin LBT battery tester and Metrohm Autolab PGSTAT302N potentiostat, respectively. All measurements were performed under ambient temperature. All specific capacities are reported per mass of graphite. Typical opencircuit potentials for the Al-graphite cells with AlCl₃:[EMIm]Cl electrolyte were ca. 1.65 V. For galvanostatic measurements, upper and lower voltage cutoff limits of 2.45 and 0.50 V were used, respectively. For each CV scan, the cell voltage was first increased to 2.45 V, decreased to 1.00 V, and then increased to the original open circuit potential.

X-ray Diffraction. An X'Pert powder X-ray diffractometer (XRD) equipped with a Cu K α radiation source ($\lambda = 0.154$ nm) was used to measure periodic structural ordering of the graphites. A scan rate of 0.5 ($^{\circ}2\theta$ /min) was used to scan a 2θ range of $20^{\circ}-60^{\circ}$.

X-ray Photoelectron Spectroscopy. A PHI Versaprobe II X-ray photoelectron spectrometer with Al K α X-rays ($h\nu$ = 1,486.6 eV, spot size = 200 μ m, 45° measuring angle) was used to analyze the composition of graphite surfaces. The source voltage and emission current were 15 kV and 4 mA, respectively. Adventitious carbon was removed from the samples via Ar+ irradiation for 10 min at 1 keV.

Deconvolution of the C 1s spectrum was performed with PHI MultiPak software using a Shirley background subtraction.

Electron Microscopy. A Zeiss Supra VP 55 scanning electron microscope (SEM) was used to image the microstructure of the graphite electrodes. ImageI software was used to measure average particle sizes. A FEI Titan Themis 200 kV transmission electron microscope (TEM) was used to probe the nanoscale structures of pristine graphites. Graphite samples were dispersed in ethanol, transferred to a TedPella lacey carbon 400 mesh grid, and then vacuum-dried at 60 °C for 2 h.

Nitrogen Sorption. N2 sorption measurements were used to measure the specific surface area of pristine graphites. Samples were degassed at 150 °C for 12 h. For NG and SG, adsorption/desorption isotherms were obtained using a Micromeritics ASAP 2020. For PG, the surface area was estimated using a Quantachrome ChemBET Pulsar via single-point Brunauer-Emmett-Teller (BET) analysis at $0.3 P/P_0$, which was more suitable due to its low specific surface area.

RESULTS AND DISCUSSION

Structural Characterization of Graphite Electrodes. Different sources and manufacturing methods of graphite yield varying structures and properties (Table 1), which influence

Table 1. Physical Properties of Pristine Graphites and Composite Graphite Electrodes

	natural (NG)	synthetic (SG)	pyrolytic (PG)				
pristine materials							
av particle size (μm)	16.5 ± 11.3	9.8 ± 7.0	27.3 ± 5.2				
bulk density (g/cm^3)	2.1	1.9	2.1				
morphology	flake-like	particle-like	lamellar sheets				
production method	mining of metaphoric rock	high-temp treatment of amorphous carbon	pyrolysis of polymeric precursors				
BET specific surface area (m^2/g)	4.4 9.3		1.0				
av crystallite height, <i>c</i> -axis (nm)	90-110	>100	10-15				
composite electrodes							
thickness (μm)	100	100	17				
porosity (%)	40	50	20				
$ \begin{array}{c} \text{conductivity} \\ \text{(S/m)} \end{array}$	660	450	5500				

their electrochemical performance in aluminum-graphite batteries. Natural graphite (NG) is extracted from metaphoric rock and then purified via thermal or chemical treatments.³⁰ Synthetic graphite (SG) is manufactured via high-temperature processing (typically >2000 °C) of amorphous carbon materials (e.g., petrochemical coke), which allows them to develop long-range ordering and large crystallite dimensions (c-axis stacking). ³¹ Pyrolytic graphite (PG) foil is typically manufactured by high-temperature pyrolysis of a polyimide precursor³² or a carbonaceous gas (e.g., acetylene).

To characterize structural differences among these graphite types, the pristine materials were analyzed using XRD, XPS, TEM, SEM, and N₂ sorption measurements. XRD patterns (Figure S1) of each type of graphite reveal similar (002) reflections associated with long-range ordering of the graphite layers. NG and SG exhibited identical interlayer d-spacings (3.38 Å), while PG had a slightly smaller d-spacing (3.36 Å). NG and SG exhibited broader (002) reflections, and minor (101) peaks were also present, likely due to larger distributions

of particle and crystal orientations³³ and/or higher c-axis crystallite dimensions $(L_c)^{34}$ compared to PG. L_c for each graphite was estimated from the literature to be lowest for PG (10-15 nm, depending on pyrolysis temperature)³⁵ and significantly higher for NG (90-110 nm, depending on particle-size fraction)³⁴ and SG (>100 nm).³¹

XPS measurements (Figure S2) were conducted on pristine NG, SG, and PG to quantify the sp² and sp³ carbon content as well as any oxygen defects on the graphite surfaces. Deconvolution of the C 1s photoelectron spectrum revealed two main peaks: (i) an asymmetric component centered at 284.0 ± 0.1 eV attributed to sp² carbons and characteristic of well-ordered graphite and (ii) a symmetric component (>90% Gaussian) centered at 285.0 ± 0.1 eV attributed to sp³ carbons associated with dangling, terminal C-C bonds at edge sites or other defects.³⁶ For all graphite types, the integrated C 1s signal areas establish that ~85% of the carbon is sp² coordinated (Table S1), indicating high crystallinity.³⁷ For NG and PG, the XPS survey spectra did not reveal any oxygen impurities. For SG, an O 1s signal was observed at 532.7 eV, which accounted for ~6% of the combined integrated area of the C 1s and O 1s signals. This O 1s signal is likely associated with C=O and/or O-C=O states³⁸ at edge sites of the SG particles.

SEM measurements were conducted to compare the morphology and particle dimensions of the composite electrodes (Figure S3). NG exhibited flake-like morphologies with average dimensions of 16.5 \pm 11.3 μ m, while SG was particle-like with average sizes of 9.8 \pm 7.0 μ m. PG was composed of lamellar sheets with average lamellar dimensions of 27.3 \pm 5.2 μ m. HR-TEM measurements (Figure S4) further confirmed the highly ordered nanoscale structures of all graphites. NG and SG exhibited high extents of periodic ordering along both the c-axis and ab-planes, while PG exhibited nanocrystalline domains with lesser extents of periodic ordering.

N₂ sorption experiments (Figure S5) established the BET specific surface areas for all graphite types, yielding 4.4, 9.3, and 1.0 m²/g for NG, SG, and PG, respectively. As expected, the surface areas of these graphites were significantly less than those of the porous carbons ($\sim 1000 \text{ m}^2/\text{g}$) typically used for supercapacitor applications.^{28,39,40}

Galvanostatic Cycling & Compositions of Al-Graphite Batteries. Device-scale galvanostatic cycling of Algraphite cells with natural, synthetic, and pyrolytic graphite electrodes revealed varying capacities and lengths of voltage plateaus due to differences in graphite structure (Figure 2). The specific discharge capacities of NG, SG, and PG electrodes were 115, 80, and 66 mAh/g, respectively (Table 2), at 60 mA/g (0.30 mA/cm²). All graphites exhibited a discharge voltage plateau at ~2.2 V that accounted for 40%, 25%, and 50% of the discharge capacity of NG, SG, and PG, respectively, as well as a lower voltage plateau at ~1.8 V. NG exhibited the greatest specific discharge capacity at all voltages compared to SG and PG as well as the highest specific discharge energy (determined by integrating the area under the voltagecapacity discharge curve), which can be partly attributed to the flake-like structure and larger lateral dimensions in the abcrystallographic plane²³ of natural graphite. For PG, covalent bonds among crystallites, 41 and possibly between graphene layers, 10 may impede interlayer expansion and explain its lower capacity.

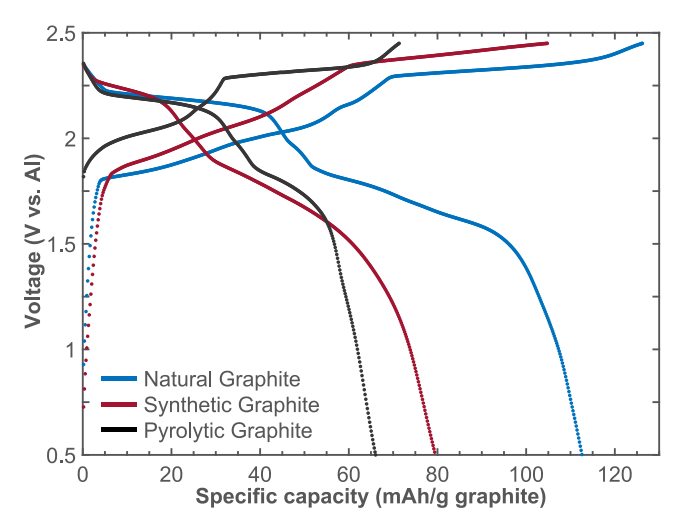


Figure 2. Galvanostatic cycling (60 mA/g) of Al-graphite cells using natural, synthetic, and pyrolytic graphite electrodes. The fifth cycle is

Table 2. Galvanostatic Discharge Properties of Al-Graphite Cells Using Different Pristine Graphites^a

	natural (NG)	synthetic (SG)	pyrolytic (PG)
discharge capacity (mAh/g) at 60 mA/g	115	80	66
discharge capacity (mAh/g) >2.2 V at 60 mA/g	45	20	30
discharge capacity retention (%) at	55	43	41

^aAll values are normalized by the mass of graphite.

During cell charging, NG, SG, and PG cells exhibited specific charge capacities of 126, 105, and 72 mAh/g, respectively, on the fifth cycle (Figure 2). Varying Coulombic efficiencies and their possible origins are discussed in the variable-rate galvanostatic cycling analyses later. The highvoltage plateau at ~2.3 V begins at approximately 56%, 52%, and 42% of the total charge capacity for NG, SG, and PG, respectively, reflecting the different extents of periodic and ordered chloroaluminate intercalation during the charge process. Note that capacity associated with surface effects, such as double-layer capacitive charging and electrochemical reactions of adsorbed species, are negligible for the graphites due to their low specific surface areas. For example, the BET specific surface areas are ~1% or less (depending on graphite type) of the available interlayer area (Text S2, Supporting Information), indicating that the capacity achieved is due to the electrochemical intercalation of chloroaluminate anions within the graphite layers.

Coulomb counting of the electrons passed during a full discharge yields the average compositions of the intercalated graphite electrodes (C_x[AlCl₄]), which vary with graphite type. For example, based on the discharge capacity of an NG electrode (115 mAh/g), the average electrode composition is C₁₉[AlCl₄] (Text S3, Supporting Information), which is similar to the results obtained by Elia et al. 12 for natural graphite electrodes. Performing the same calculation for SG and PG electrodes yields average stoichiometries of C28[AlCl4] and C₃₄[AlCl₄], respectively. This estimation does not consider any intercalated AlCl₄⁻ species that may be "trapped" within the graphite layers. ¹⁶ For the NG electrode, the experimental capacity of the first charge is 160 mAh/g (discussed below). While this additional capacity (compared to 115 mAh/g) may be due to a combination of irreversible side reactions (e.g., electrolyte degradation) and trapped ions, it is informative to estimate the composition in the limit where all additional capacity is due solely to trapped ions. Under these assumptions, the average composition of the intercalated NG electrode would be C₁₄[AlCl₄]. The actual concentration of AlCl₄ within NG is thus between C₁₉[AlCl₄] and C₁₄[AlCl₄].

Cyclic Voltammetry & Graphite Staging. Cyclic voltammetry was performed on Al-graphite cells to elucidate further insights into the electrochemical differences among the graphite types (Figure 3). A slow CV scan rate (20 μ V/s) was used to reduce diffusion limitations and to obtain highresolution voltammograms.⁴² Both the first scan (red, dashed traces) and third scan (black traces) are shown as well as the background signal from a Mo/electrolyte/Mo cell (Figure 3a, dashed black trace). Third scan CVs, which capture electrochemical processes that occur beyond the initial cycle, are discussed first and then compared to the first scan.

The CV peaks show potential-specific reactions associated with the electrochemical intercalation of chloroaluminate anions, which correspond to different stages of intercalation. 10,16,22,43-45 Staging refers to the periodic ordering by which ions intercalate within the graphite interlayers; a stage number n is the average number of graphene layers between intercalated layers. From the open circuit potential (ca. 1.65 V), increasing the voltage up to \sim 1.85 V results in intercalation of ions, which is reported to be stage 6 according to Pan et al.^{22,44} (using *in operando* XRD and DFT) calculations or stages 8–4 by Childress et al.^{22,44} (using *in situ* Raman). Further increasing the potential up to \sim 2.0 V is suggested to yield stage 5 by Pan et al. 22,44 or stages 4–2 by Childress et al. 22,44 Scanning up to ~2.35 V results in the most intense oxidation peak corresponding to the highest intercalation density achievable at room temperature, which has been reported by in operando XRD measurements for SP-1 natural graphite to be stage 4 by Pan et al. 44 and stage 3 by Wang et al. 45 Using ex situ XRD, Zhang et al. 23 reported stage 4 and Chen et al. 13 reported either stage 3 or stage 4 for various graphene-like film electrodes. Note that Pan et al.44 also observed an additional CV peak at ~2.5-2.6 V when the temperature was decreased to −10 °C, which was reported to be stage 3 intercalation. Using in situ Raman spectroscopy, Childress et al.²² reported that the ~2.4 V oxidation peak corresponded to stage 1 intercalation for few-layered graphene foam electrodes. Also, by using in situ Raman spectroscopy, Angell et al. 46 reported that fully charged natural graphite using the AlCl₃:urea electrolyte system was intercalated to stage 2. Thus, the maximum intercalation stage achievable depends on a combination of the graphite structure and temperature, while the stage numbers reported vary by characterization method.

The average stage number of the fully intercalated graphite can also be estimated by comparing the average composition $C_r[AlCl_4]$, determined coulometrically from the experimentally measured capacity, to the theoretical composition at a given stage number and AlCl₄ packing density. By use of a hardsphere packing model (Text S4, Supporting Information), which assumes that the AlCl₄⁻ ions are rigid, noninteracting spheres with 2D hexagonal packing, the maximum composition is $C_{9,3}[AlCl_4]$. If one uses this model as a first approximation, an ideal stage 1 and stage 2 intercalated graphite would have capacities of 240 and 120 mAh/g, respectively, where the latter

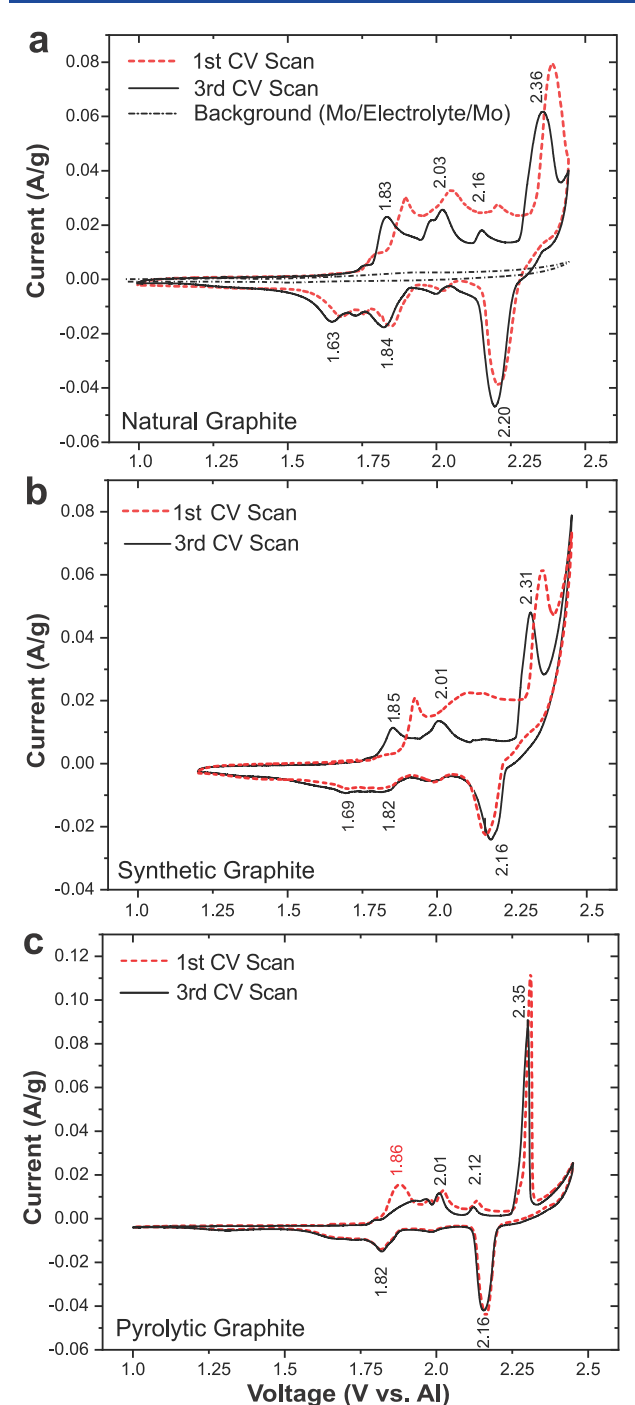


Figure 3. Representative cyclic voltammograms (20 μ V/s) for aluminum cells with (a) natural, (b) synthetic, and (c) pyrolytic graphite electrodes. A CV of a Mo–Mo symmetric cell is displayed in (a), showing the weak background associated with bare Mo current collectors.

represents an average composition of $C_{18.6}[AlCl_4]$ (Text S4, Supporting Information). As mentioned above, NG exhibited a discharge capacity of 115 mAh/g, or an average composition of $C_{19}[AlCl_4]$, which are very close to the theoretical capacity and composition of ideal stage 2 intercalated graphite by using the hard-sphere model. Effects of ion trapping, as discussed above, would increase the expected $AlCl_4^-$ content and thus decrease the average stage number toward stage 1. The actual packing density of $AlCl_4^-$ ions within the graphite layers will depend

upon molecular-level interactions between the $AlCl_4^-$ ions and bounding graphene layers as well as among the $AlCl_4^-$ ions themselves. DFT electronic structure calculations of different $AlCl_4^-$ interlayer packing densities indicate that high interlayer packing densities are more energetically favorable compared to more dilute ones and that a range of interlayer compositions may be possible. ⁴⁷

Currently, there are discrepancies between the stage numbers of fully charged graphites determined by XRD methods, Raman spectroscopy, and coulometric-geometric models. XRD methods only measure structures with sufficient long-range ordering to diffract X-rays and often ignore problems of indeterminacy. For example, as Read⁴⁸ has previously shown for PF₆⁻ anion intercalation into graphite, it is difficult to unambiguously determine the stage number via XRD studies alone because it is possible for intercalated graphites to have identical unit cell dimensions in the dimension perpendicular to the graphite planes (c-axis) but exhibit different staging. Meanwhile, DFT and geometric models assume idealized structures. Real graphites exhibit edge sites, steps, and basal planes, as well as defects and disorder, all of which can affect the specific capacity but are not accounted for in the above models or structures. Reconciling these discrepancies would provide opportunities to clarify the structure and composition of the chloroaluminate-intercalated graphite electrodes as well as the role of defects and disorder.

As the CV is further scanned up to 2.45 V, a sharp increase of oxidative current occurs that is associated with irreversible electrochemical reactions, e.g., electrolyte decomposition. Specifically, the electrochemical oxidation of AlCl₄⁻ to form Al₂Cl₇⁻ and Cl₂ gas,⁴⁹ along with possible chlorination of the graphite to form C–Cl bonds at edge sites, defects, and/or particle surfaces,^{16,28} may be occurring. Among the different graphites, SG exhibited the strongest oxidative current at 2.45 V (Figure 3). The greater current associated with irreversible reactions is likely due to SG's higher oxygen content (Figure S2) as well as its higher specific surface area and consequently greater concentrations of edge sites, which are more reactive than basal plane sites.⁵⁰ PG exhibited the lowest extents of decomposition reactions at 2.45 V, likely due to its low specific surface area and stacked lamellar sheets morphology, which reduces active site utilization⁵¹ and therefore surface reactivity.

Upon reversal of the CV direction to discharge the cell, the major reduction peak occurring at ~2.2 V corresponds to anion deintercalation. Further scanning yields lower voltage redox peaks at ~1.80 and ~1.60 V, which correspond to more dilute, less-coordinated staging of anions (increasing stage numbers n). The stage number n of the discharge (reduction) peaks is expected to be similar to their corresponding charge (oxidation) peaks. The reduction peaks occur at a lower voltage compared to the corresponding oxidation peaks. Analysis of the potential difference between the oxidation and reduction peaks ($\Delta E_{\rm peak} = E_{\rm peak}^{\rm ox} - E_{\rm peak}^{\rm red}$) revealed that all coupled redox processes were of a quasi-reversible nature.⁵² For the higher voltage (\sim 2.3 V/ \sim 2.15 V) couple, ΔE_{peak} was 160, 150, and 190 mV for NG, SG, and PG, respectively. The large separation between these coupled peaks suggests hysteresis in the equilibrium voltage and/or a large activation overpotential. 52,53 Lower-voltage coupled peaks observed in all three graphite types were 1.84 V/2.03 V (NG), 1.82 V/2.01 V (SG), and 1.82 V/2.01 V (PG), which all had an even greater ΔE_{peak} (~200 mV), indicative of the large voltage hysteresis between the intercalation/deintercalation processes. This

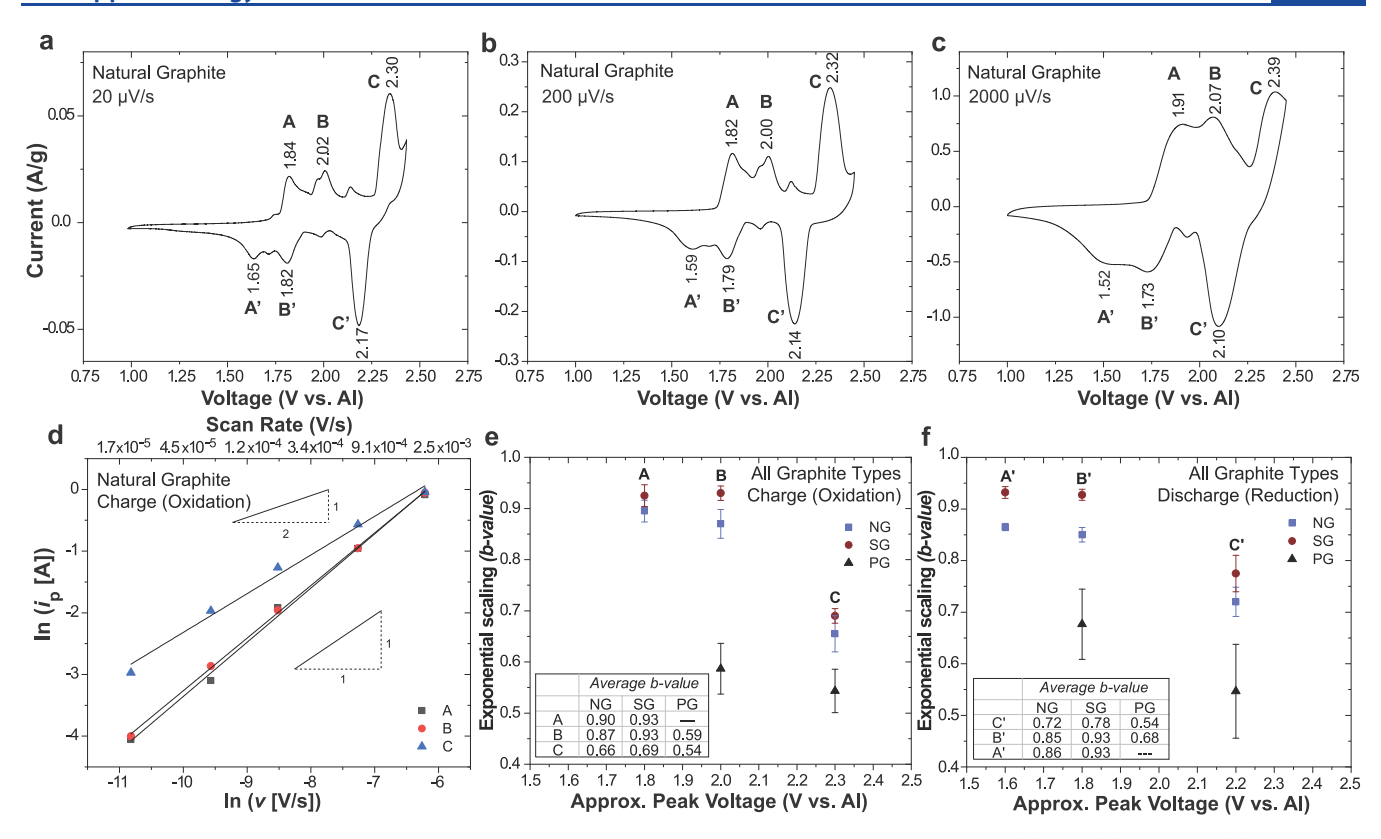


Figure 4. Variable-rate cyclic voltammograms performed on an Al-natural graphite cell at scan rates of (a) 20, (b) 200, and (c) 2000 μ V/s. Coupled charge (oxidation) peaks and discharge (reduction) peaks are labeled A-C and A'-C', respectively. Note that A (A') peaks were not observed for PG. (d) Peak current (i_p) vs scan rate (ν) fit to a power-law model (eq 3). (e) Exponential scaling term (b-value) for the oxidation and (f) reduction peaks as a function of potential for all graphite types. Measurements were performed on three different cells for each graphite type; uncertainty bars represent the standard deviation about the mean value.

larger peak separation suggests that broader distributions of intercalation stage transitions 13,22 occur in this voltage range, which is consistent with the highly sloping charge (\sim 2.0 V) and discharge (\sim 1.8 V) plateaus observed in the galvanostatic cycling curve (Figure 2).

Other interesting electrochemical differences among the graphites were revealed by CV. For example, the integrated CV area in the 1.80-2.25 V range relative to the area of the entire voltammogram was greatest for NG, then lower for SG, and lowest for PG. This observation suggests that structural features of NG results in facile dilute-stage intercalation. Note that NG exhibits sharper, better defined CV peaks than SG in this region, which suggests that NG exhibits more uniform intercalation environments. 43 Similarly, PG also exhibited fewer discrete lower voltage peaks associated with dilute staging, possibly due to its smaller crystallite domains (Figure S4). Consequently, for PG, the current response of the high-voltage oxidation peak at 2.3 V is ~1 order of magnitude larger than the other low-intensity peaks. Thus, electrochemical intercalation of chloroaluminate anions occurs only once the potential is high enough, resulting in a greater current density because the graphite interlayers were relatively vacant before the higher cell voltage was established.

Differences between the first (initial) and third (steadystate) CVs reveal insights on the structural changes associated with "initializing" the electrode for reversible chloroaluminate intercalation, a process which requires intercalating ions to overcome the cohesive van der Waals forces between adjacent graphite layers. Overlays of the first and subsequent voltammograms (Figure 3) showed that the oxidative peaks of the first CV scan (red) are more intense and broader than those in the subsequent cathodic scan (black). This observation can be attributed to the higher activation barrier for the electroactive species to initially penetrate the unopened graphite interlayers.

For NG and SG, the oxidation peaks of the initial CV scan at $\sim\!1.9,\sim\!2.1$, and $\sim\!2.4$ V shifted to lower voltages (by $\sim\!0.5\!-\!1.0$ V) in the third scan, which also decreased $\Delta E_{\rm peak}$. The shift to lower voltages upon intercalation suggests increased electrochemical reversibility (e.g., enhanced mass transfer and/or more facile electron transfer) after the first scan. Also, for PG, the initial oxidation peak observed at 1.86 V corresponding to the onset of ordered staging 10,16 disappeared in subsequent CV scans due to significant ion trapping, 10,16 which indicates incomplete reversal of intercalation staging during cell discharge.

Quantifying Ionic Transport Limitations of Chloroaluminate Intercalation. Variable-rate CVs were conducted and analyzed to understand how mass transfer affects the rate of chloroaluminate electrochemical intercalation. Diffusion-limited and reaction-limited electrochemical processes can be quantitatively distinguished by analyzing how the peak current scales with scan rate in variable-rate cyclic voltammograms. The peak current i_p typically obeys a power-law relationship the sweep rate ν according to

$$i_{\rm p} = av^b \tag{2}$$

The exponential scaling term b can be determined by fitting the linearized expression:

$$\ln(i_{p}) = b \ln(v) + \ln(a) \tag{3}$$

In a completely diffusion-limited regime, the current is proportional to the square root of the scan rate $(i_p \sim v^{0.5})$. For intercalation electrodes, diffusion-limited currents are typically due to the slow solid-state diffusion of ions within the host structure. Physically, any ions occupying intercalation sites at the interface must first diffuse into the host structure for such sites to once again become available for electrochemical intercalation—the process that generates current. Note that this solid-state diffusion process is much slower compared to the diffusive transport of ions to the electrode surface from the bulk electrolyte solution.

Conversely, when the current scales linearly with the scan rate $(i_p \sim v^1)$, such electrochemical processes are not diffusionlimited. For example, faradaic electrochemical reactions of adsorbed species on the electrode surface are effectively reaction-limited and consequently exhibit linear scaling relationships.⁵² Non-faradaic capacitive charging of the electrical double layer can also exhibit similar linear scaling behavior.⁵² Here, because of the low specific surface areas of the graphites tested (Table 1), the current is dominated by electrochemical intercalation, and any surface effects are considered negligible (Text S2, Supporting Information). Any deviations from a square-root scaling thus imply that the intercalation process is simply not diffusion-limited.

Indeed, Levi and Aurbach⁵³ observed two distinct regimes for lithium-ion intercalation into thin-film graphite electrodes when analyzing variable-rate CVs: (i) a well-defined linear regime $(i_p \sim v^1)$ at very slow scan rates ($\leq 15 \,\mu\text{V/s}$) due to the quasi-steady-state, non-diffusion-controlled accumulation of lithium ions within the graphitic electrodes and (ii) a welldefined diffusion-limited region $(i_p \sim v^{0.5})$ at faster scan rates $(\geq 15 \ \mu V/s)$ associated with semi-infinite solid-state diffusion of lithium ions within the graphite layers. As shown below, variable-rate CV analyses of Al-graphite cells establish markedly different behavior for chloroaluminate anion intercalation into graphite compared to lithium cation

Variable-rate CV measurements (20, 70, 200, 700, and 2000 $\mu V/s$) were performed on the Al-graphite batteries (Figure 4a-c for NG; see Figure S6 for complete data on NG, SG, and PG). The CVs were acquired from low to high scan rates; the third scans are shown and analyzed. The current of coupled oxidation (reduction) peaks at approximately 1.8 (1.6) V, 2.0 (1.8) V, and 2.3 (2.2) V (respectively labeled A (A'), B (B'), and C(C') were analyzed as a function of scan rate according to eq 3, which yielded linear relationships ($R^2 > 0.97$) between $ln(i_p)$ and ln(v) (Figure 4d for NG, Figure S7 for all graphite types). The exponential scaling term (b-value) for oxidation (charge) and reduction (discharge) peaks for all graphite types is shown in Figure 4e and 4f, respectively.

The exponential scaling relationships vary significantly as a function of potential and among graphite types, establishing unambiguously that ion intercalation associated with different potentials and graphite structure influence the mass transport regime. Notably, for natural and synthetic graphite, lower voltage peaks exhibited scaling relationships of approximately $i_{\rm p} \sim v^{0.9}$; for example, NG and SG respectively had mean bvalues of 0.90 (0.86) and 0.93 (0.93) for A (A') peaks and values of 0.87 (0.85) and 0.93 (0.93) for B (B') peaks. Thus, the electrochemical intercalation of molecular chloroaluminate anions into graphite is not diffusion-limited at these potentials,

but effectively reaction-limited. Subsequent oxidation (charging) to >2.3 V, which results in electrochemical intercalation to the densest graphite staging achievable at room temperature, is a process more diffusion-limited in character. Reduction (discharging) to <2.1 V results in electrochemical deintercalation processes with similar extents of transport limitations. For example, NG and SG exhibited mean b values of 0.66 (0.72) and 0.69 (0.78) for the C (C') peaks (or approximately $i_p \sim v^{0.7}$), respectively. For PG, electrochemical intercalation of chloroaluminates is more diffusion-limited compared to NG and SG, since PG exhibited mean b-values of 0.59 (0.68) for its B (B') peaks and 0.54 (0.54) for its C (C') peaks. This result may be a consequence of the higher concentrations of nanocrystalline grain boundaries within PG, as measured by HR-TEM (Figure S4), which impede ion diffusion.

Variable-rate CV analyses thus establish that the electrochemical intercalation of molecular chloroaluminate anions into graphite operates within a fundamentally different mass transport regime compared to lithium cation intercalation. Exponential scaling relationships ranged from approximately i_p $\sim v^{0.9}$ at lower voltages (1.8 to 2.1 V during charge) and $i_p \sim$ $v^{0.7}$ at higher voltages (>2.3 V during charge) over rates from 20 μ V/s to 2 mV/s compared to classic $i_p \sim \nu^{0.5}$ diffusion-limited scaling for lithium cations at rates >15 μ V/s.⁵³ Notably, in the aluminum-graphite system, both solid-state ion diffusion and the rate of electrochemical intercalation at the electrode-electrolyte interface (i.e., the coupled ion insertion and charge transfer events) play a key role in controlling the overall current. The departure from a completely diffusioncontrolled process may be attributed to (i) "fast" solid-state diffusion of chloroaluminate ions within the graphite structure and/or (ii) "slow" interfacial electrochemical intercalation of molecular ions (AlCl₄⁻). The ultrahigh rate performance of many engineered graphites, compared to pristine graphites, is likely attributed to reduced mass transfer limitations (e.g., reduced ion diffusion length scales, as in graphitic foams), which partially control the overall rate of intercalation as we have shown.

We highlight fundamental differences between the aluminum-graphite and lithium-graphite systems that are expected to affect their overall rate capabilities. With regards to electrochemical intercalation at the electrode-electrolyte interface, we note that there is currently no evidence in the literature of a passivating interphase forming on the graphite electrode with chloroaluminate-containing ionic liquids, 56 unlike the solid electrolyte interphase (SEI) that is well-known to form in lithium-ion batteries with organic electrolytes.⁵⁷ Such an SEI would add a mass-transfer resistance to electrochemical intercalation at the interface. In addition, there are relatively weak ion-ion interactions within the AlCl₃/[EMIm]Cl electrolyte⁵⁸ and hence weak desolvation penalties for AlCl₄⁻ intercalation. Both the absence of an SEI and weak ion desolvation penalties would be expected to enhance ion intercalation at the interface. Note that the kinetics of the electron charge transfer between AlCl₄ and graphite have not been measured to date. While not expected to be rate limiting, they must be quantified to understand their effects, if any.

With regards to solid-state ion diffusion, the lower charge density and larger size of molecular AlCl₄ anions, compared to the higher charge density and smaller size of atomic Li⁺ cations, will affect their diffusive behavior. Lower ion charge density reduces interactions between the intercalated ions and

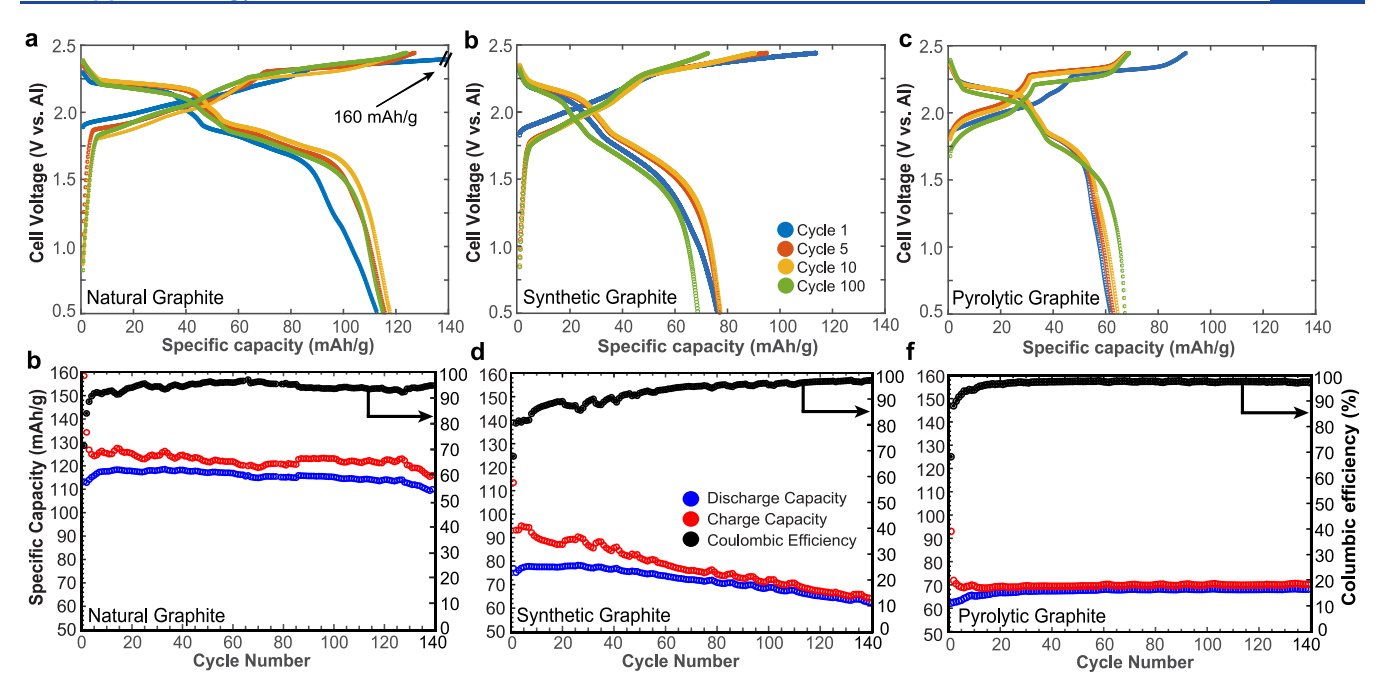


Figure 5. Long-term galvanostatic cycling (60 mA/g) and the resulting capacities and Coulombic efficiencies of rechargeable aluminum—graphite cells with (a, b) natural graphite, (c, d) synthetic graphite, and (e, f) pyrolytic graphite electrodes.

the graphite layers and is expected to enhance diffusion, while conversely, larger ion size is expected to slow diffusion. In addition, the intercalation of larger molecular ions may open a larger interlayer spacing for subsequent ions to diffuse. Any ion trapping that occurs during the initial cycles would amplify this effect. We hypothesize that the large size of the intercalated molecular anions may also restrict their penetration depths at lower potentials (<2.1 V), mitigating solid-state diffusion limitations (as measured here). Higher potentials (>2.3 V) are then required for the sterically bulky molecular anions to overcome the local cohesive van der Waals forces between graphene layers before they can diffuse farther into the graphite particles.

Long-Term Al-Graphite Battery Performance. Extended galvanostatic cycling (60 mA/g) demonstrated varying degrees of electrochemical irreversibility that contributed to capacity fade among NG, SG, and PG (Figure 5). For the first cycle, elevated charge capacity and low Coulombic efficiency (~70%) were observed for all graphites. This effect is attributed to a combination of electrolyte degradation reactions as well as ion trapping, both of which are more pronounced during the first cycle. By the fifth cycle, the main discharge plateaus are longer and flatter (Figure 5a,c,e).

The graphites showed different extents of capacity fade and changes in Coulombic efficiency. NG, SG, and PG exhibited a 10%, 22%, and 2% discharge capacity fade (compared to the maximum discharge capacity) over 140 cycles, respectively (Figure 5b,d,f). SG exhibited the greatest discharge capacity fade, likely due to its higher surface area and thus greater concentration of edge sites. Furthermore, SG's oxygen content (~6 at. %) (XPS, Figure S2) suggests a higher concentration of dangling carbon bonds at the edge sites, 38 which are more reactive and thus more likely to catalyze irreversible decomposition reactions. Interestingly, the Coulombic efficiency of SG increased from 80% on cycle 2 to 98% at cycle 100, although accompanied by a shortened discharge plateau at 2.2 V. This effect may be partly attributed to two effects: (i) in

situ graphite exfoliation⁶⁰ during cycling, due to the mechanical stress associated with repeated (de)intercalation of the chloroaluminate anions, and (ii) reduced magnitude of any graphite chlorination reactions, which have been reported to occur and may be more prevalent at reactive edge sites.^{44,61} NG, in contrast, did not exhibit this increase in Coulombic efficiency. PG maintained stable voltage profiles and capacity (Figure 5e) as well as Coulombic efficiency (98.0%) (Figure 5f).

To evaluate the extent of anion trapping and electrolyte degradation reactions occurring near 2.45 V, a separate set of galvanostatic cycling experiments were conducted where a reduced upper voltage limit (2.30 V, as opposed to 2.45 V) was used for the first 20 cycles of galvanostatic cycling. 62 The initial Coulombic efficiency was significantly higher (~88%) and rapidly increased to ~98% by the 20th cycle for all types of graphite. NG (Figure 6) and SG (Figure S8) did not exhibit charge/discharge plateaus at 2.3 V/2.1 V corresponding to high-density intercalation/deintercalation, while PG still achieved a portion of its typical high-voltage charge and discharge plateaus (Figure S8). Beyond the first 20 galvanostatic cycles, the voltage limit was increased to 2.45 V. Immediately thereafter, the Coulombic efficiency dropped slightly for PG and more significantly for NG and SG. This behavior may be due to ion trapping and/or electrolyte degradation. If ion trapping is indeed occurring, then it occurs when chloroaluminate anions intercalate during the higher voltage charge plateaus, as seen in the galvanostatic profiles (Figure 6b and Figure S8c,d) and the corresponding dQ/dVpeak (Figure 6c and Figure S8e,f). Another benefit observed from initially using a 2.30 V upper voltage limit was the improved discharge capacity and cycling stability, even for subsequent cycles that used a 2.45 V voltage cutoff. For example, after 140 cycles, the capacity fade was negligible for NG and only 13% for SG.

Rate-Dependent Al-Graphite Battery Performance. Galvanostatic cycling was performed at rates from 60 to 3840

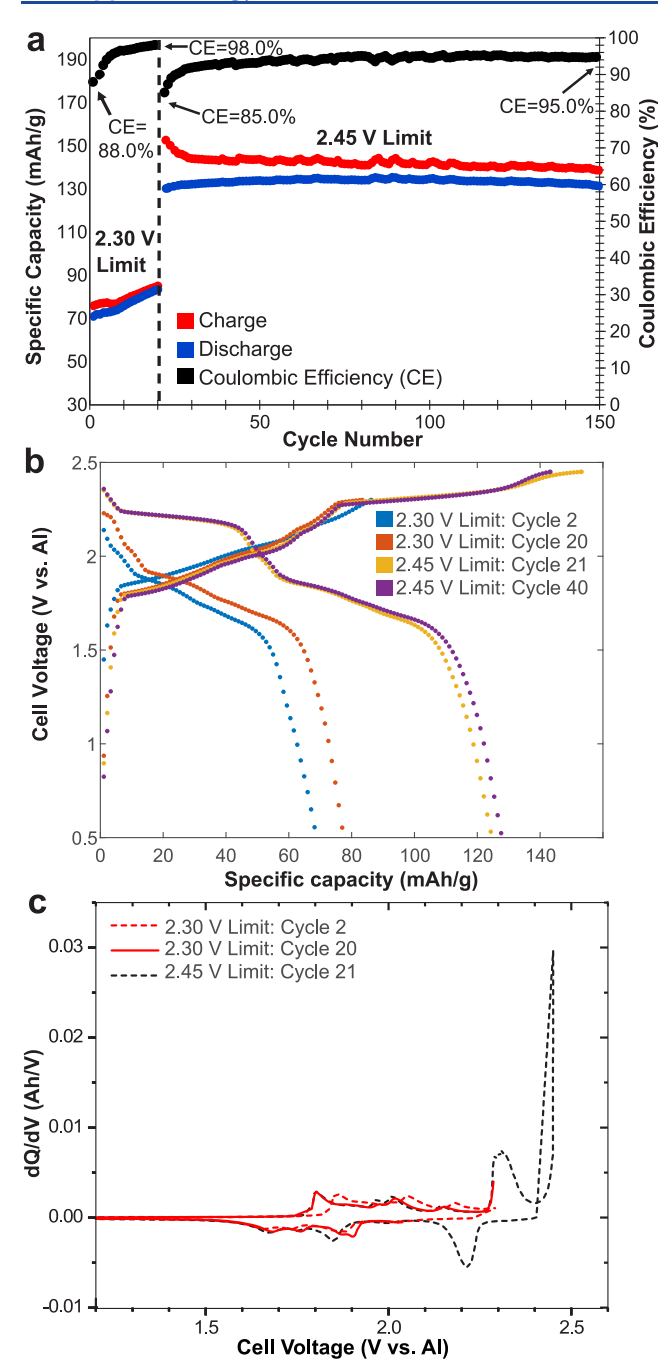


Figure 6. Improved performance of Al–natural graphite cells can be achieved by using a reduced upper voltage limit of 2.30 V for the initial 20 cycles, then raising it to 2.45 V. (a) Galvanostatic cycling, (b) cyclic voltammetry, and (c) differential capacity (dQ/dV) plots are shown for natural graphite. Data for synthetic and pyrolytic graphites are shown in Figure S8.

mA/g (Figure 7) to further study the rate dependence of voltage profiles, capacities, and Coulombic efficiencies of the Al—graphite cells. Capacities decreased when the current densities increased, as expected, because the diffusive penetration depth of chloroaluminate anions within the graphite layers was limited over the available intercalation/deintercalation time, and thus full capacity was not achievable. NG has the highest capacity retention at all rates. Discharge capacity retention at 240 mA/g was 93%, 75%, and 85% for NG, SG, and PG, respectively, and 55%, 41%, and 42% at 960

mA/g (Table 2). At 960 mA/g, NG retained a small portion of its high-voltage discharge plateau at 2.25 V (~10 mAh/g), while this plateau vanished for SG and PG. At the maximum cycling rate tested (3840 mA/g), both NG and SG retained 20% of its initial discharge capacity, while PG only retained 4%. The greater capacity retention of NG and SG at higher current densities, compared to PG, is corroborated by reduced ion diffusion limitations, as measured in the variable-rate CV analyses discussed above. The poorer rate performance of PG, compared to that of NG and SG, may also be due to additional mass transfer resistances associated with diffusion across nanocrystalline grain boundaries, as revealed by HR-TEM (Figure S4). Both electrochemical cycling techniques thus provide complementary quantitative comparisons of how mass transport affects the rate of electrochemical intercalation of chloroaluminate species among the three graphite types, which correlate with their rate performance.

For all graphites, the Coulombic efficiency increased when the rates increased, as the irreversible electrochemical reactions (e.g., electrolyte reactions¹⁶) were kinetically suppressed. For example, the Coulombic efficiency was 98.9%, 96.1%, and 98.2% for NG, SG, and PG at 240 mA/g and 99.9%, 99.8%, and 99.3% at 960 mA/g. These results highlight that the reversible electrochemical intercalation of chloroaluminates into graphite is a more rapid process compared to the irreversible electrochemical processes that degrade battery performance. When the current density was returned to 60 mA/g after the 125th cycle, the capacity increased and the Coulombic efficiency decreased to their previous values, which indicated that cycling stability was maintained even after subjecting the graphites to rapid (de)intercalation of molecular chloroaluminate anions.

CONCLUSIONS

Rechargeable aluminum-graphite batteries containing natural, synthetic, and pyrolytic graphite electrodes were electrochemically analyzed, yielding insights into the effects of graphite structure and ion transport on performance. Natural graphite exhibited the highest specific capacity (115 mAh/g at 60 mA/ g) at all potentials and the greatest capacity retention during variable-rate galvanostatic cycling (e.g., 55% at 960 mA/g). Cyclic voltammograms (20 μ V/s) revealed that lower voltage (<2.1 V) redox processes associated with low-density graphite staging were most prominent for natural graphite, while the dominant charge storage mechanism for all graphites was reversible chloroaluminate intercalation/deintercalation (~2.3 V/2.2 V) at the highest density achievable at room temperature. Average compositions of fully intercalated electrodes were determined coulometrically; for example, fully intercalated natural graphite has a composition of C₁₉[AlCl₄], neglecting trapped anions during first charge. With regard to graphite staging, we highlight discrepancies among different methods and models used in the literature and analyze ideal staging using a hard-sphere model.

Both CV and galvanostatic analyses establish that the extent of irreversible electrochemical reactions (e.g., electrolyte degradation), and hence Coulombic efficiency, depend strongly on the nature of the graphite. Synthetic graphite exhibited the lowest Coulombic efficiency, likely due to its higher specific surface area and greater concentrations of both edge sites and oxygen surface defects. Pyrolytic graphite exhibited the best Coulombic efficiency and hence long-term cycling stability. Long-term cycling of all Al—graphite cells can

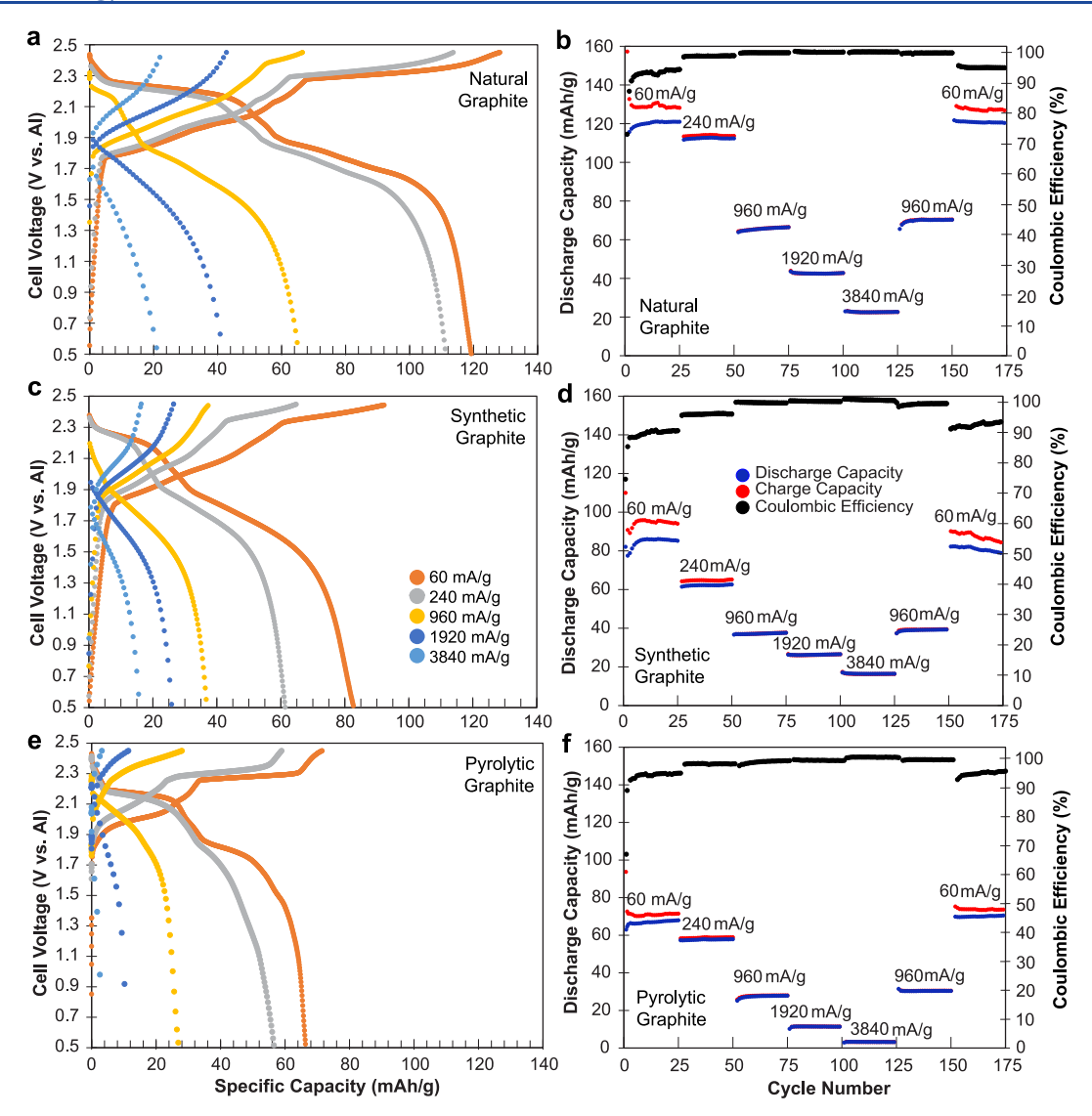


Figure 7. Variable-rate galvanostatic cycling curves, capacities, and Coulombic efficiencies at rates from 60 to 3840 mA/g for aluminum-graphite cells with (a, b) natural graphite, (c, d) synthetic graphite, and (e, f) pyrolytic graphite electrodes.

be improved by lowering the upper voltage limit to 2.3 V for the initial cycles. Improvements to the Coulombic efficiency of the Al-graphite cells at slower cycling rates, which depend strongly upon graphite structure, could be made by identifying the mechanisms of deleterious side reactions and mitigating them by, for example, developing alternative electrolytes or appropriately pretreating the graphite.

Variable-rate CV measurements were analyzed to understand quantitatively how the rates of electrochemical chloroaluminate (de)intercalation are affected by ion mass transport limitations. For both natural and synthetic graphites, intercalation/deintercalation at voltages <2.1 V was effectively reaction-limited ($i_{\rm p} \sim v^{0.9}$), while higher voltage intercalation/ deintercalation at ~2.3 V/2.2 V was neither strongly diffusion-nor reaction-limited ($i_p \sim v^{0.7}$). Among different graphite structures, pyrolytic graphite exhibited the greatest extents of diffusion limitations for all cell potentials. Electrochemical intercalation of molecular chloroaluminate anions thus differs significantly from the intercalation of lithium cations, which has been shown by Levi and Aurbach⁵³ to be diffusion-controlled ($i_p \sim v^{0.5}$) over similar scan rates (>15 μ V/s). Collectively, these results are a first step toward understanding

the excellent rate capabilities of rechargeable aluminumgraphite batteries in chloroaluminate-containing ionic liquids.

ASSOCIATED CONTENT

S Supporting Information

The Supporting Information is available free of charge on the ACS Publications website at DOI: 10.1021/acsaem.9b01184.

XRD, XPS, SEM, TEM and N2 sorption measurements of pristine graphites, variable-rate CVs and scaling analyses for all graphites, long-term galvanostatic cycling with different voltage limits for synthetic and pyrolytic graphites, and additional calculations (PDF)

AUTHOR INFORMATION

Corresponding Author

*E-mail: rmessinger@ccny.cuny.edu.

Jeffrey H. Xu: 0000-0003-3404-4194 Damon E. Turney: 0000-0003-1759-1735 Ankur L. Jadhav: 0000-0002-6481-4084 Robert J. Messinger: 0000-0002-5537-3870

Notes

The authors declare no competing financial interest.

ACKNOWLEDGMENTS

The authors gratefully acknowledge support from the U.S. National Science Foundation under Grant CBET-1706926 as well as the Imaging and Surface Science Facilities of the CUNY Advanced Science Research Center.

REFERENCES

- (1) Erickson, E. M.; Ghanty, C.; Aurbach, D. New Horizons for Conventional Lithium Ion Battery Technology. J. Phys. Chem. Lett. 2014, 5, 3313-3324.
- (2) Linden, D.; Reddy, T. B. Handbook of Batteries; McGraw-Hill: 2002.
- (3) Shkolnikov, E. I.; Zhuk, A. Z.; Vlaskin, M. S. Aluminum as Energy Carrier: Feasibility Analysis and Current Technologies Overview. Renewable Sustainable Energy Rev. 2011, 15, 4611-4623.
- (4) Zafar, Z. A.; Imtiaz, S.; Razaq, R.; Ji, S.; Huang, T.; Zhang, Z.; Huang, Y.; Anderson, J. A. Cathode Materials for Rechargeable Aluminum Batteries: Current Status and Progress. J. Mater. Chem. A 2017, 5, 5646-5660.
- (5) Zhang, M.; Song, X.; Ou, X.; Tang, Y. Rechargeable Batteries Based on Anion Intercalation Graphite Cathodes. Energy Storage Mater. 2019, 16, 65-84.
- (6) Das, S. K.; Mahapatra, S.; Lahan, H. Aluminium-Ion Batteries: Developments and Challenges. J. Mater. Chem. A 2017, 5, 6347-
- (7) Elia, G. A.; Marquardt, K.; Hoeppner, K.; Fantini, S.; Lin, R.; Knipping, E.; Peters, W.; Drillet, J. F.; Passerini, S.; Hahn, R. An Overview and Future Perspectives of Aluminum Batteries. Adv. Mater. 2016, 28, 7564-7579.
- (8) Zhao, Y.; VanderNoot, T. J. Electrodeposition of Aluminium from Nonaqueous Organic Electrolytic Systems and Room Temperature Molten Salts. Electrochim. Acta 1997, 42, 3-13.
- (9) Gifford, P. R.; Palmisano, J. B. An Aluminum/Chlorine Rechargeable Cell Employing a Room Temperature Molten Salt Electrolyte. J. Electrochem. Soc. 1988, 135, 650-654.
- (10) Lin, M.-C.; Gong, M.; Lu, B.; Wu, Y.; Wang, D.-Y.; Guan, M.; Angell, M.; Chen, C.; Yang, J.; Hwang, B.-J.; Dai, H. An Ultrafast Rechargeable Aluminium-Ion Battery. Nature 2015, 520, 324-328.
- (11) Sun, H.; Wang, W.; Yu, Z.; Yuan, Y.; Wang, S.; Jiao, S. A New Aluminium-Ion Battery with High Voltage, High Safety and Low Cost. Chem. Commun. 2015, 51, 11892-11895.
- (12) Elia, G. A.; Kyeremateng, N. A.; Marquardt, K.; Hahn, R. An Aluminum/Graphite Battery with Ultra-High Rate Capability. Batter. Supercaps 2018, 2, 83-90.
- (13) Chen, H.; Xu, H.; Wang, S.; Huang, T.; Xi, J.; Cai, S.; Guo, F.; Xu, Z.; Gao, W.; Gao, C. Ultrafast All-Climate Aluminum-Graphene Battery with Quarter-Million Cycle Life. Sci. Adv. 2017, 3, No. eaao7233.
- (14) Wu, Y.; Gong, M.; Lin, M.-C. C.; Yuan, C.; Angell, M.; Huang, L.; Wang, D.-Y. Y.; Zhang, X.; Yang, J.; Hwang, B.-J. J.; Dai, H. 3D Graphitic Foams Derived from Chloroaluminate Anion Intercalation for Ultrafast Aluminum-Ion Battery. Adv. Mater. 2016, 28, 9218-
- (15) Mckerracher, R. D.; Holland, A.; Cruden, A.; Wills, R. G. A. Comparison of Carbon Materials as Cathodes for the Aluminium-Ion Battery. Carbon 2019, 144, 333-341.
- (16) Elia, G. A.; Hasa, I.; Greco, G.; Diemant, T.; Marquardt, K.; Hoeppner, K.; Behm, R. J.; Hoell, A.; Passerini, S.; Hahn, R. Insights into the Reversibility of Aluminum Graphite Batteries. J. Mater. Chem. A **2017**, *5*, 9682–9690.
- (17) Wang, S.; Kravchyk, K. V.; Krumeich, F.; Kovalenko, M. V. Kish Graphite Flakes as a Cathode Material for an Aluminum Chloride-Graphite Battery. ACS Appl. Mater. Interfaces 2017, 9, 28478-28485.

- (18) Wang, D.; Wei, C.; Lin, M.; Pan, C.; Chou, H.; Chen, H.; Gong, M.; Wu, Y.; Yuan, C.; Angell, M.; Hsieh, Y.; Chen, Y.; Wen, C.; Chen, C.; Hwang, B.; Chen, C.; Dai, H. Advanced Rechargeable Aluminium Ion Battery with a High-Quality Natural Graphite Cathode. Nat. Commun. 2017, 8, 1-7.
- (19) Huang, M.-C.; Yang, C.-H.; Chiang, C.-C.; Chiu, S.-C.; Chen, Y.-F.; Lin, C.-Y.; Wang, L.-Y.; Li, Y.-L.; Yang, C.-C.; Chang, W.-S. Influence of High Loading on the Performance of Natural Graphite-Based Al Secondary Batteries. Energies 2018, 11, 2760.
- (20) Rani, J. V.; Kanakaiah, V.; Dadmal, T.; Rao, M. S.; Bhavanarushi, S. Fluorinated Natural Graphite Cathode for Rechargeable Ionic Liquid Based Aluminum - Ion Battery. J. Electrochem. Soc. 2013, 160, A1781-A1784.
- (21) Kravchyk, K. V.; Wang, S.; Piveteau, L.; Kovalenko, M. V. Efficient Aluminum Chloride-Natural Graphite Battery. Chem. Mater. 2017, 29, 4484-4492.
- (22) Childress, A. S.; Parajuli, P.; Zhu, J.; Podila, R.; Rao, A. M. A Raman Spectroscopic Study of Graphene Cathodes in High-Performance Aluminum Ion Batteries. Nano Energy 2017, 39, 69-76.
- (23) Zhang, L.; Chen, L.; Luo, H.; Zhou, X.; Liu, Z. Large-Sized Few-Layer Graphene Enables an Ultrafast and Long-Life Aluminum-Ion Battery. Adv. Energy Mater. 2017, 7, 1700034.
- (24) Chen, H.; Guo, F.; Liu, Y.; Huang, T.; Zheng, B.; Ananth, N.; Xu, Z.; Gao, W.; Gao, C. A Defect-Free Principle for Advanced Graphene Cathode of Aluminum-Ion Battery. Adv. Mater. 2017, 29, 1605958.
- (25) Xu, H.; Bai, T.; Chen, H.; Guo, F.; Xi, J.; Huang, T.; Cai, S.; Chu, X.; Ling, J.; Gao, W.; Xu, Z.; Gao, C. Low-Cost AlCl₃/Et₃NHCl Electrolyte for High-Performance Aluminum-Ion Battery. Energy Storage Mater. 2019, 17, 38-45.
- (26) Yu, X.; Wang, B.; Gong, D.; Xu, Z.; Lu, B. Graphene Nanoribbons on Highly Porous 3D Graphene for High-Capacity and Ultrastable Al-Ion Batteries. Adv. Mater. 2017, 29, 1604118.
- (27) Zhang, C.; He, R.; Zhang, J.; Hu, Y.; Wang, Z.; Jin, X. Amorphous Carbon Derived Nanosheets-Bricked Porous Graphite as High Performance Cathode for Aluminum-Ion Batteries. ACS Appl. Mater. Interfaces 2018, 10, 26510-26516.
- (28) Stadie, N. P.; Wang, S.; Kravchyk, K. V.; Kovalenko, M. V. Zeolite-Templated Carbon as an Ordered Microporous Electrode for Aluminum Batteries. ACS Nano 2017, 11, 1911-1919.
- (29) Huang, X.; Liu, Y.; Zhang, H.; Zhang, J.; Noonan, O.; Yu, C. Free-Standing Monolithic Nanoporous Graphene Foam as a High Performance Aluminum-Ion Battery Cathode. J. Mater. Chem. A 2017, 5, 19416-19421.
- (30) Tamashausky, A. V. An Introduction to Synthetic Graphite; Asbury Graphite Mills Inc.: 2006.
- (31) Wissler, M. Graphite and Carbon Powders for Electrochemical Applications. J. Power Sources 2006, 156, 142-150.
- (32) Venkatachalam, S.; Depriester, M.; Sahraoui, A. H.; Capoen, B.; Ammar, M. R.; Hourlier, D. Thermal Conductivity of Kapton-Derived Carbon. Carbon 2017, 114, 134-140.
- (33) Badenhorst, H. Microstructure of Natural Graphite Flakes Revealed by Oxidation: Limitations of XRD and Raman Techniques for Crystallinity Estimates. Carbon 2014, 66, 674-690.
- (34) Ishii, T.; Kaburagi, Y.; Yoshida, A.; Hishiyama, Y.; Oka, H.; Setoyama, N.; Ozaki, J.-i.; Kyotani, T. Analyses of Trace Amounts of Edge Sites in Natural Graphite, Synthetic Graphite and High-Temperature Treated Coke for the Understanding of Their Carbon Molecular Structures. Carbon 2017, 125, 146-155.
- (35) Hirai, T.; Yajima, S. Structural Features of Pyrolytic Graphite. J. Mater. Sci. 1967, 2, 18-27.
- (36) Blume, R.; Rosenthal, D.; Tessonnier, J. P.; Li, H.; Knop-Gericke, A.; Schlögl, R. Characterizing Graphitic Carbon with X-Ray Photoelectron Spectroscopy: A Step-by-Step Approach. ChemCatChem 2015, 7, 2871-2881.
- (37) Lesiak, B.; Kövér, L.; Tóth, J.; Zemek, J.; Jiricek, P.; Kromka, A.; Rangam, N. C Sp2/Sp3 Hybridisations in Carbon Nanomaterials - XPS and (X)AES Study. Appl. Surf. Sci. 2018, 452, 223-231.

- (38) Phaner-Goutorbe, M.; Sartre, A.; Porte, L. Soft Oxidation of Graphite Studied by XPS and STM. *Microsc., Microanal., Microstruct.* **1994**, *5*, 283–290.
- (39) Yang, G. Y.; Chen, L.; Jiang, P.; Guo, Z. Y.; Wang, W.; Liu, Z. P. Fabrication of Tunable 3D Graphene Mesh Network with Enhanced Electrical and Thermal Properties for High-Rate Aluminum-Ion Battery Application. *RSC Adv.* **2016**, *6*, 47655–47660.
- (40) Ji, L.; Meduri, P.; Agubra, V.; Xiao, X.; Alcoutlabi, M. Graphene-Based Nanocomposites for Energy Storage. *Adv. Energy Mater.* **2016**, *6*, 1502159.
- (41) Greco, G.; Tatchev, D.; Hoell, A.; Krumrey, M.; Raoux, S.; Hahn, R.; Elia, G. A. Influence of the Electrode Nano/Microstructure on the Electrochemical Properties of Graphite in Aluminum Batteries. *J. Mater. Chem. A* **2018**, *6*, 22673–22680.
- (42) Aurbach, D.; Markovsky, B.; Weissman, I.; Levi, E.; Ein-Eli, Y. On the Correlation between Surface Chemistry and Performance of Graphite Negative Electrodes for Li Ion Batteries. *Electrochim. Acta* 1999, 45, 67–86.
- (43) Dresselhaus, M. S.; Dresselhaus, G. Intercalation Compounds of Graphite. *Adv. Phys.* **2002**, *51*, 1–186.
- (44) Pan, C.-J.; Yuan, C.; Zhu, G.; Zhang, Q.; Huang, C.-J.; Lin, M.-C.; Angell, M.; Hwang, B.-J.; Kaghazchi, P.; Dai, H. An Operando X-Ray Diffraction Study of Chloroaluminate Anion-Graphite Intercalation in Aluminum Batteries. *Proc. Natl. Acad. Sci. U. S. A.* **2018**, *115*, 5670–5675.
- (45) Wang, D.-Y.; Huang, S.-K.; Liao, H.-J.; Chen, Y.-M.; Wang, S.-W.; Kao, Y.-T.; An, J.-Y.; Lee, Y.-C.; Chuang, C.-H.; Huang, Y.-C.; Lu, Y.-R.; Lin, H.-J.; Chou, H.-L.; Chen, C.-W.; Lai, Y.-H.; Dong, C.-L. Insights into Dynamic Molecular Intercalation Mechanism for Al C Battery by Operando Synchrotron X-Ray Techniques. *Carbon* 2019, 146, 528–534.
- (46) Angell, M.; Pan, C.-J.; Rong, Y.; Yuan, C.; Lin, M.-C.; Hwang, B.-J.; Dai, H. High Coulombic Efficiency Aluminum-Ion Battery Using an AlCl3-Urea Ionic Liquid Analog Electrolyte. *Proc. Natl. Acad. Sci. U. S. A.* **2017**, *114*, 834–839.
- (47) Gao, Y.; Zhu, C.; Chen, Z.; Lu, G. Understanding Ultrafast Rechargeable Aluminum-Ion Battery from First-Principles. *J. Phys. Chem. C* 2017, 121, 7131–7138.
- (48) Read, J. A. In-Situ Studies on the Electrochemical Intercalation of Hexafluorophosphate Anion in Graphite with Selective Cointercalation of Solvent. *J. Phys. Chem. C* **2015**, *119*, 8438–8446.
- (49) Carlin, R. T.; Crawford, W.; Bersch, M. Nucleation and Morphology Studies of Aluminum Deposited from an Ambient-Temperature Chloroaluminate Molten Salt. J. Electrochem. Soc. 1992, 139, 2720
- (50) Hennig, G. R. Anisotropic Reactivities of Graphite—I. Reactions of Ozone and Graphite. *Carbon* **1965**, *3*, 107–114.
- (51) Wang, P.; Chen, H.; Li, N.; Zhang, X.; Jiao, S.; Song, W. L.; Fang, D. Dense Graphene Papers: Toward Stable and Recoverable Al-Ion Battery Cathodes with High Volumetric and Areal Energy and Power Density. *Energy Storage Mater.* **2018**, *13*, 103–111.
- (52) Bard, A. J.; Faulkner, L. R. Electrochemical Methods: Fundamentals and Applications, 1944.
- (53) Levi, M. D.; Aurbach, D. The Mechanism of Lithium Intercalation in Graphite Film Electrodes in Aprotic Media. Part 1. High Resolution Slow Scan Rate Cyclic Voltammetric Studies and Modeling. *J. Electroanal. Chem.* **1997**, 421, 79–88.
- (54) Wang, J.; Polleux, J.; Lim, J.; Dunn, B. Pseudocapacitive Contributions to Electrochemical Energy Storage in TiO ₂ (Anatase) Nanoparticles. *J. Phys. Chem. C* **2007**, *111*, 14925–14931.
- (55) Lindström, H.; Södergren, S.; Solbrand, A.; Rensmo, H.; Hjelm, J.; Hagfeldt, A.; Lindquist, S.-E. Li⁺ Ion Insertion in TiO₂ (Anatase). 2. Voltammetry on Nanoporous Films. *J. Phys. Chem. B* **1997**, *101*, 7717–7722.
- (56) Zafar, Z. A.; Imtiaz, S.; Li, R.; Zhang, J.; Razaq, R.; Xin, Y.; Li, Q.; Zhang, Z.; Huang, Y. A Super-Long Life Rechargeable Aluminum Battery. *Solid State Ionics* **2018**, 320, 70–75.
- (57) An, S. J.; Li, J.; Daniel, C.; Mohanty, D.; Nagpure, S.; Wood, D. L. The State of Understanding of the Lithium-Ion-Battery Graphite

- Solid Electrolyte Interphase (SEI) and Its Relationship to Formation Cycling. *Carbon* **2016**, *105*, 52–76.
- (58) Kamath, G.; Narayanan, B.; Sankaranarayanan, S. K. R. S. Atomistic Origin of Superior Performance of Ionic Liquid Electrolytes for Al-Ion Batteries. *Phys. Chem. Chem. Phys.* **2014**, *16*, 20387–20391.
- (59) Wu, M. S.; Xu, B.; Chen, L. Q.; Ouyang, C. Y. Geometry and Fast Diffusion of AlCl₄ Cluster Intercalated in Graphite. *Electrochim. Acta* **2016**, *195*, 158–165.
- (60) Lei, H.; Tu, J.; Yu, Z.; Jiao, S. Exfoliation Mechanism of Graphite Cathode in Ionic Liquids. ACS Appl. Mater. Interfaces 2017, 9, 36702–36707.
- (61) Schlögl, R. Graphite A Unique Host Lattice. *Phys. Chem. Mater. Low-Dimens. Struct.* **1994**, 17, 83–176.
- (62) Shi, J.; et al. Avoiding Pitfalls in Rechargeable Aluminum Batteries Research. ACS Energy Lett. 2019, 4, 2124—2129.

Supporting Information

Effects of Graphite Structure and Ion Transport on the Electrochemical Properties of Rechargeable Aluminum-Graphite Batteries

Jeffrey H. Xu, Damon E. Turney, Ankur Jadhav, Robert J. Messinger*

Department of Chemical Engineering, The City College of New York, CUNY, New York, New York 10031, United States *E-mail: rmessinger@ccny.cuny.edu

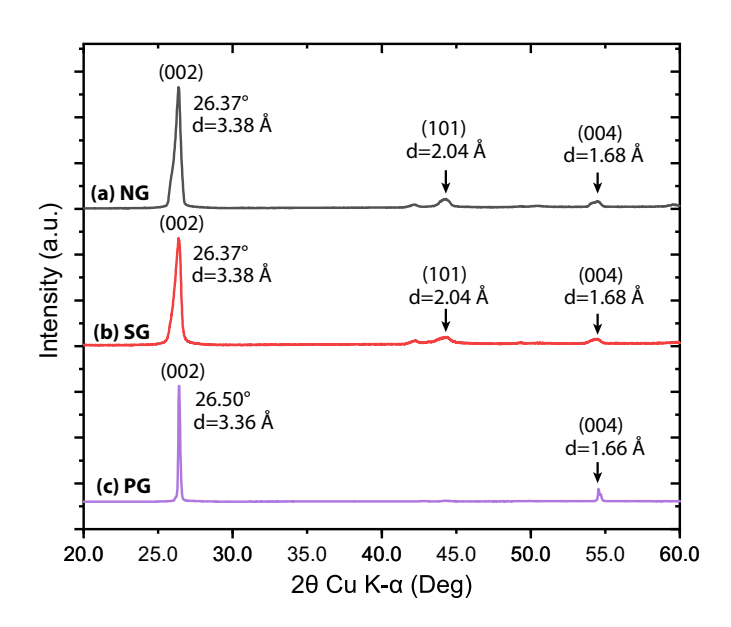


Figure S1. X-Ray diffraction (XRD) patterns for pristine (a) natural graphite (NG), (b) synthetic graphite (SG) and (c) pyrolytic graphite (PG).

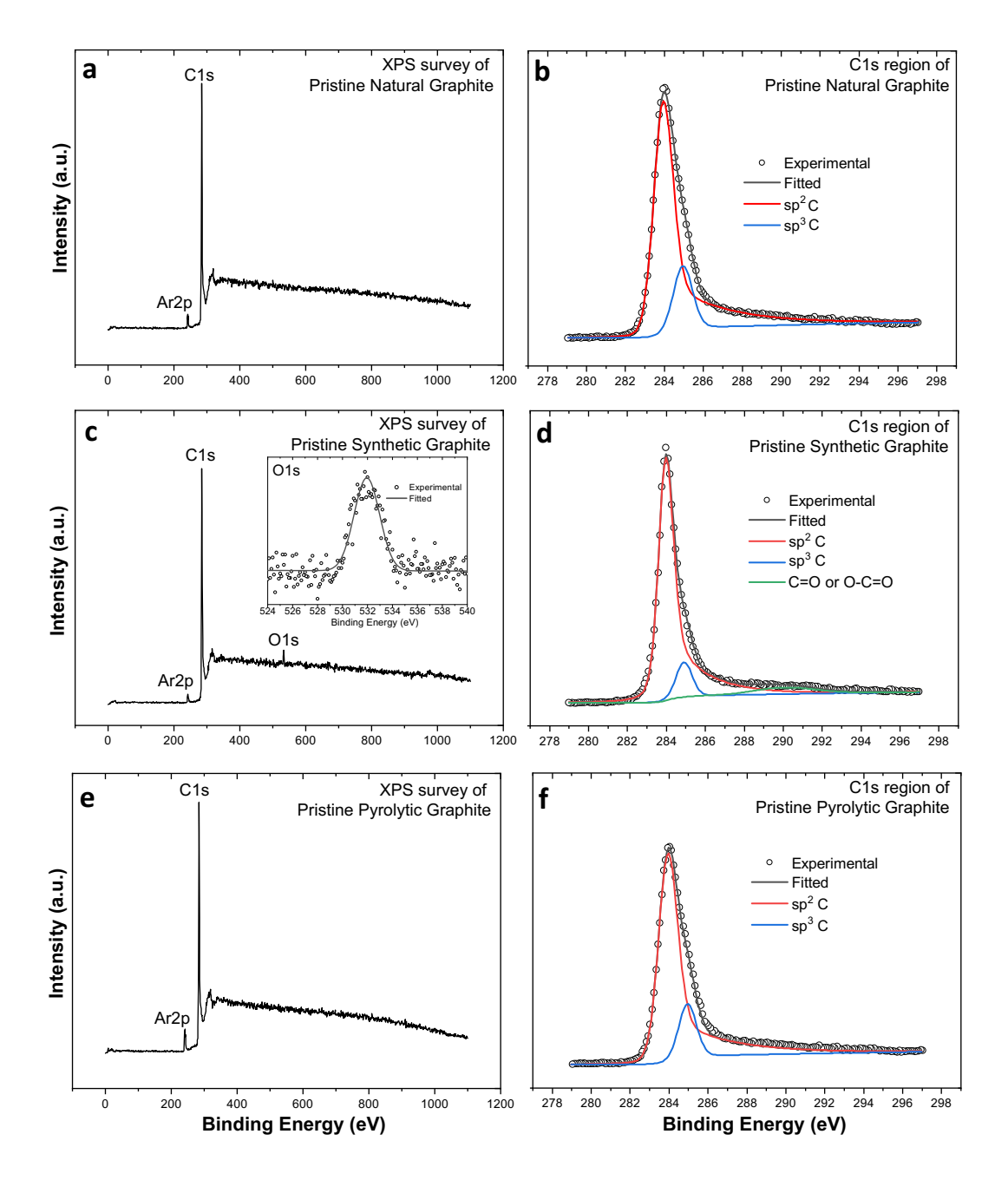


Figure S2. X-ray photoelectron (XPS) survey and deconvoluted C1s spectra of pristine (a,b) natural graphite, (c,d) synthetic graphite (inset: fitted O1s region), and (e,f) pyrolytic graphite. Concentrations (atomic %) are based on signal intergration of C1s components are tabulated in Table S1.

Table S1. Concentrations of carbon and oxygen states obtained by quantitative deconvolution of XPS C1s signals.

Graphite Type	Atomic %			Chi-Squared (χ²)
	C sp ²	C sp ³	C=O & O-C=O	
	(284.0 ± 0.1 eV)	(285.0 ± 0.1 eV)	(289.9 eV)	
Natural	85.2	14.8	-	1.95
Synthetic	84.3	9.0	6.7	5.37
Pyrolytic	83.9	16.1	-	2.38

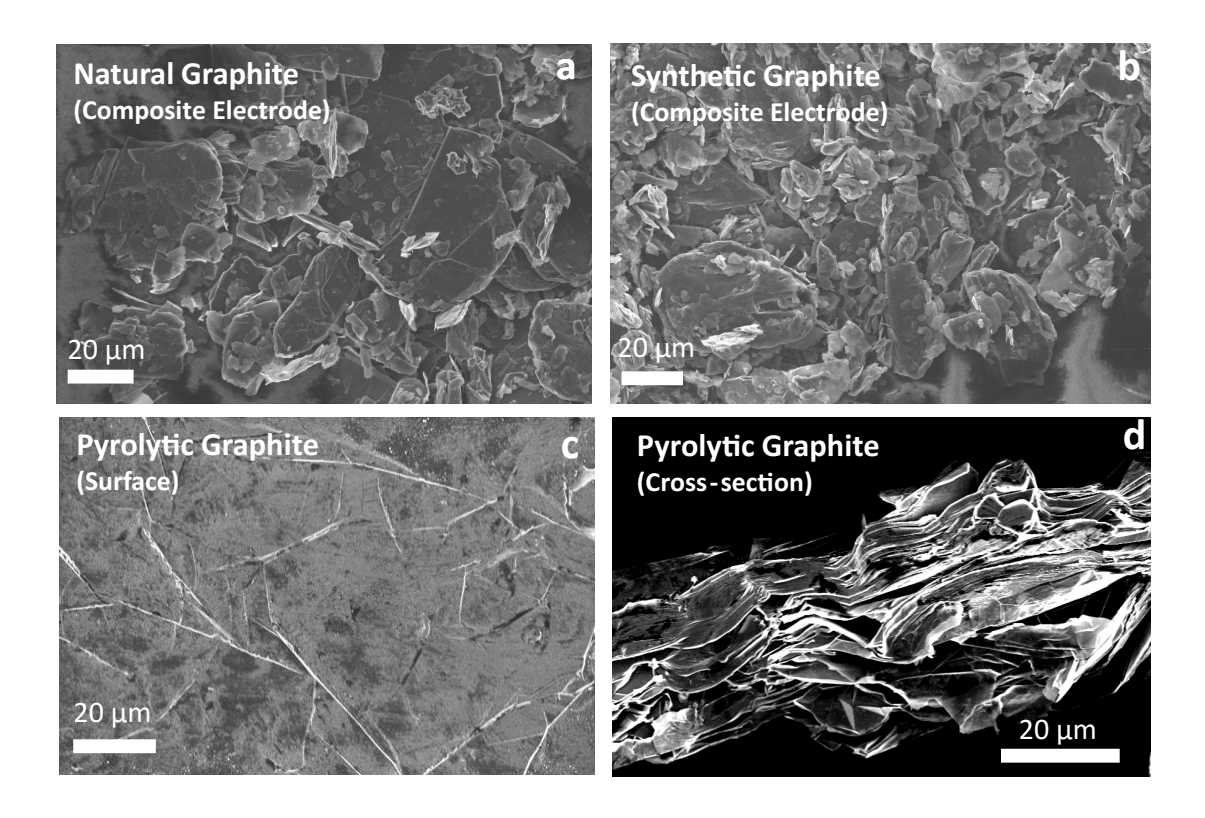


Figure S3. Scanning electron microscopy (SEM) images of a (a) natural graphite composite electrode, (b) synthetic graphite composite electrode, and (c,d) pristine pyrolytic graphite foil.

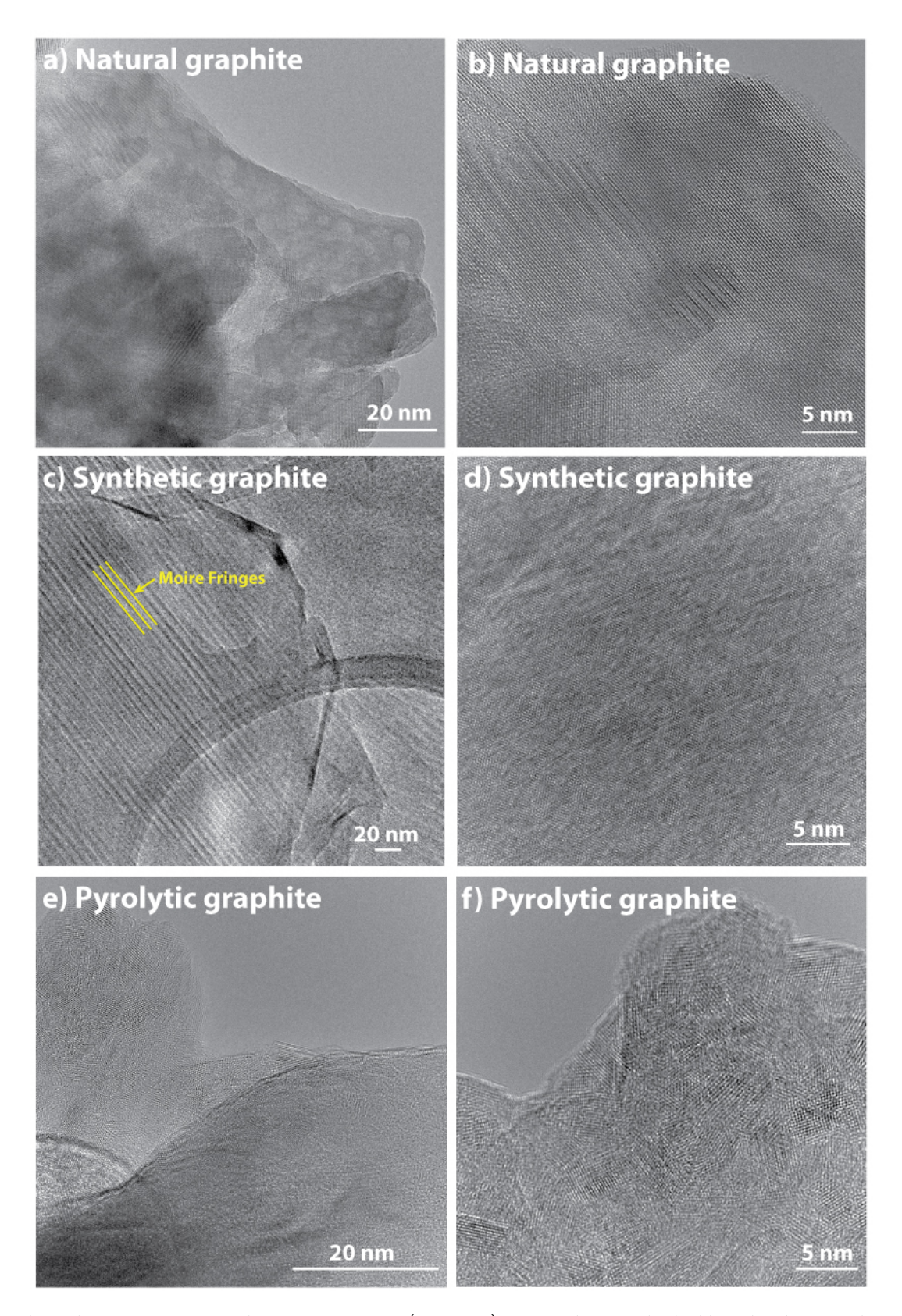


Fig S4. High-resolution transmission electron microscopy (HR-TEM) images showing the highly-ordered nanoscale structures of pristine (a,b) natural graphite, (c,d) synthetic graphite, and (e,f) pyrolytic graphite.

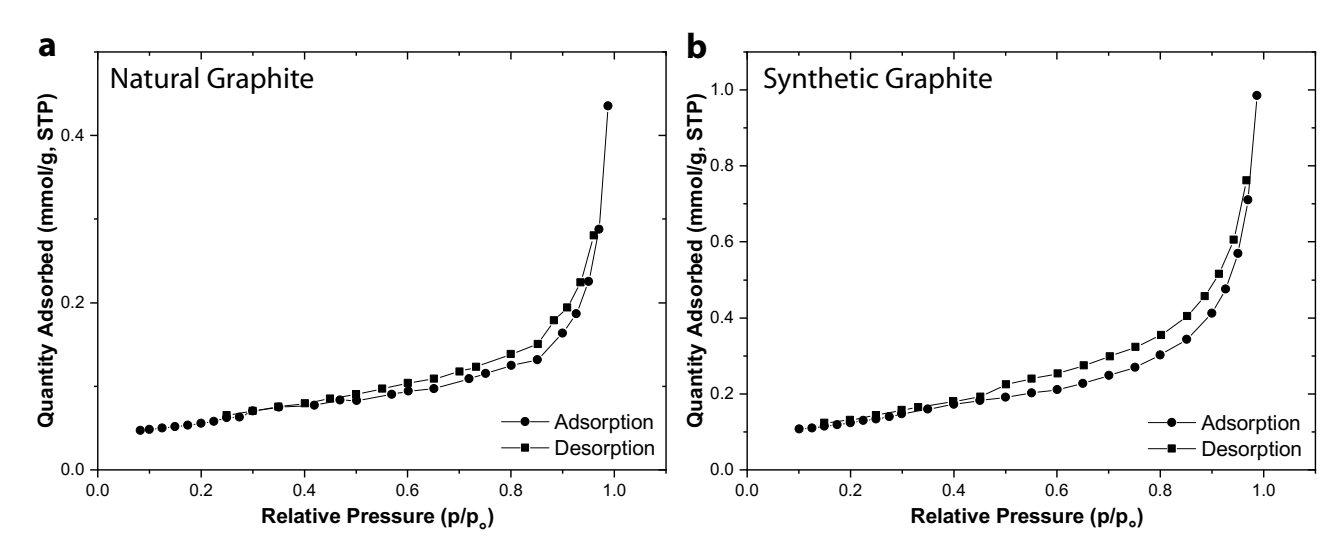


Figure S5. Nitrogen sorption isotherms for pristine (a) natural graphite and (b) synthetic graphite. No isotherm was obtained for pyrolytic graphite due to its low specific surface area, which was estimated via single-point BET analysis conducted at $P/P_0 = 0.3$.

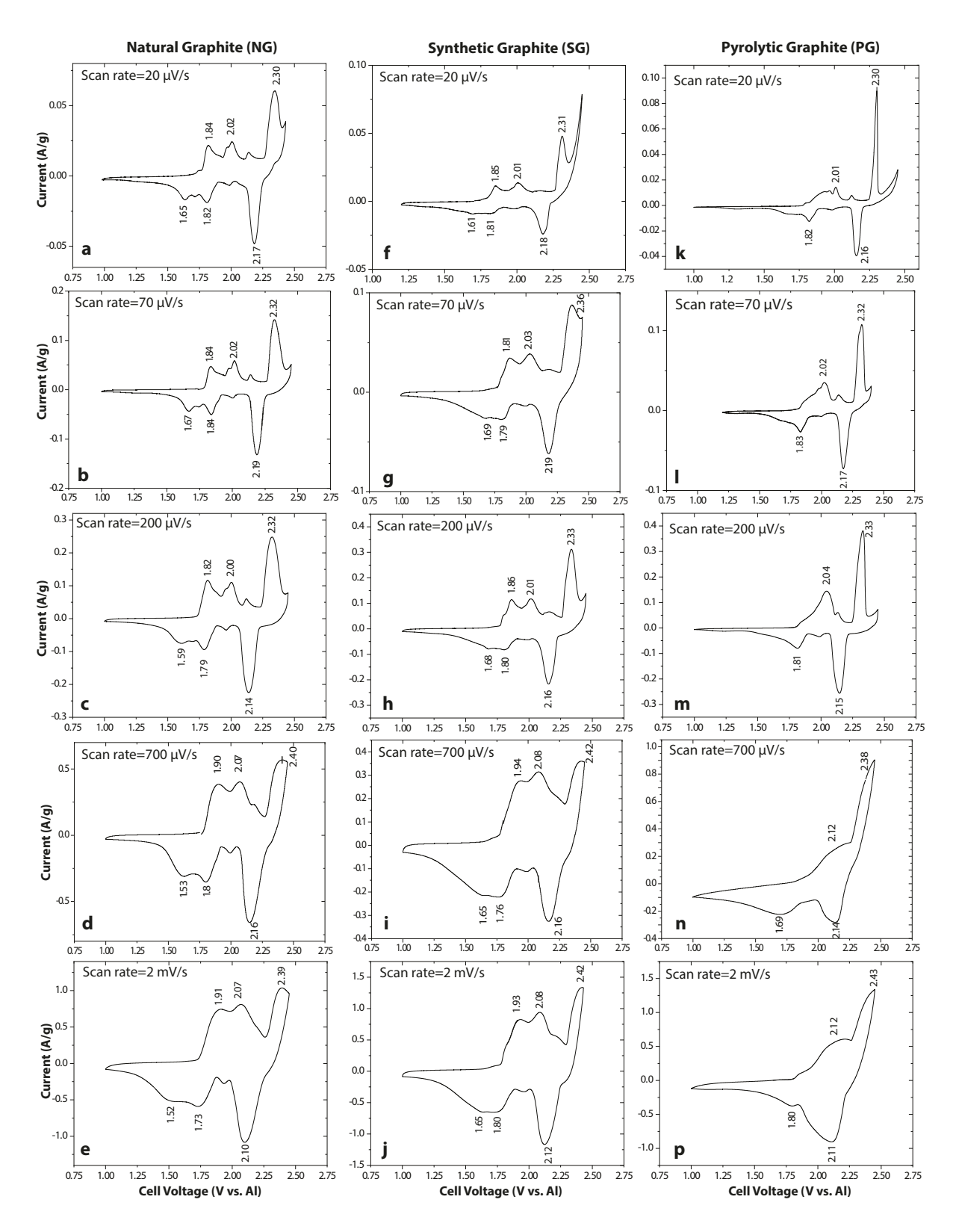


Figure S6. Variable scan-rate cyclic voltammograms (CVs) of representative Al-graphite cells with (a-e) natural graphite, (f-j) synthetic graphite, and (k-p) pyrolytic graphite at scan rates ranging from $20 \,\mu\text{V/s}$ to $2 \,\text{mV/s}$.

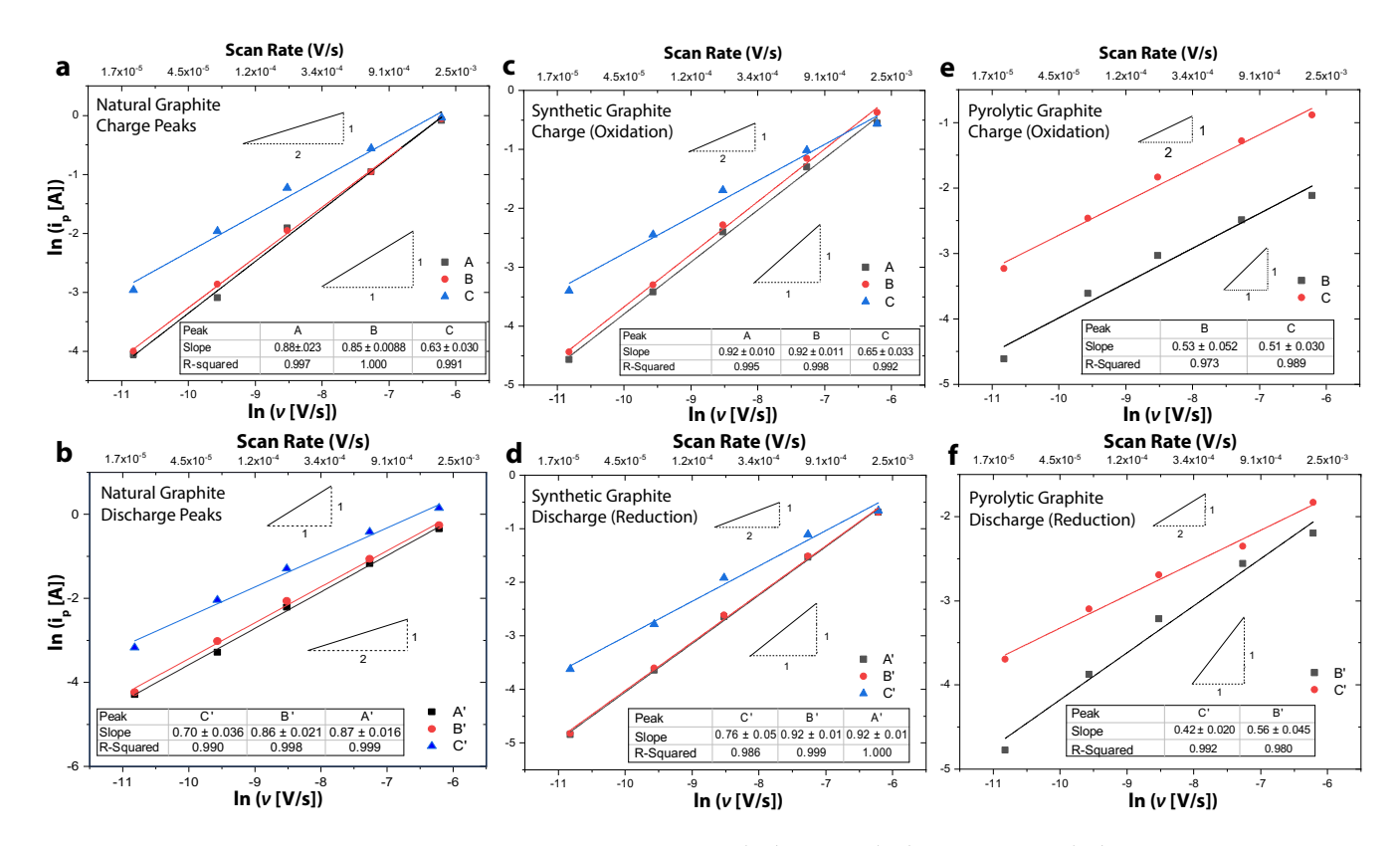


Figure S7. Variable-rate analyses of CV data for on Al-graphite cells with (a,b) natural, (c,d) synthetic, and (e,f) pyrolytic graphites. Peak current vs. scan rate data was fit to a power law model (Eqn. 3, main text). Exponential scaling term (b-value) for the oxidation and reduction peaks as a function of potential are shown as insets. Measurements were performed on three different cells for each graphite type; one representative trial is shown here.

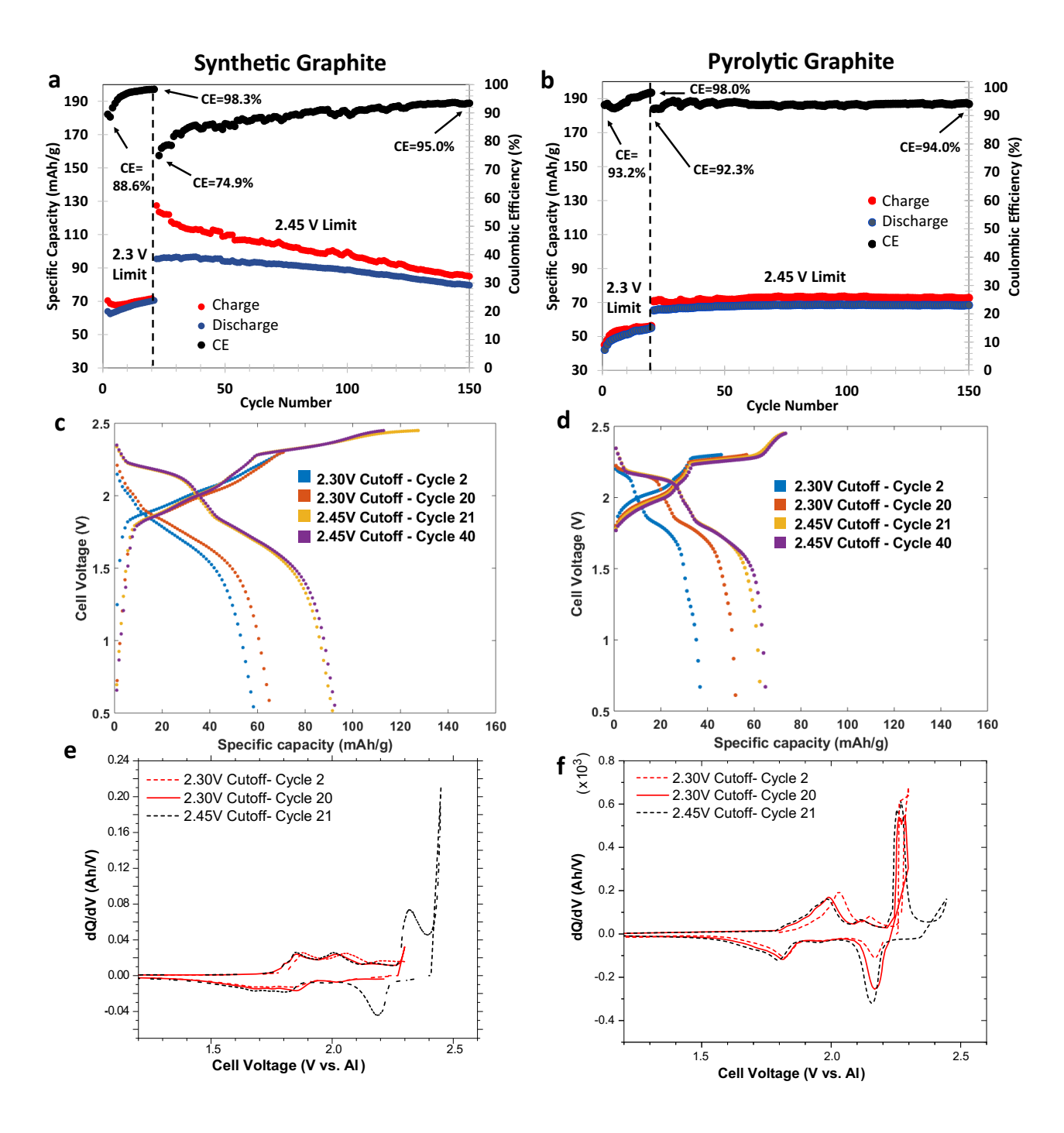


Figure S8. Electrochemical performance of Al-graphite cells with synthetic graphite (SG) and pyrolytic graphite (PG), where a reduced voltage limit of 2.30 V was used for the first 20 cycles and subsequently raised to 2.45 V on cycle 21 and after, improving long-term coulombic efficiency. (a,b) Galvanostatic cycling, (c,d) cyclic voltammetry, and (e,f) differential capacity (dQ/dV) plots are shown for (a,c,e) synthetic graphite and (b,d,f) pyrolytic graphite.

Supporting Text & Calculations

Text S1. Calculation of the porosity of the composite electrodes:

The porosities of the composite natural & synthetic graphite composite electrodes were estimated according to:

% Porosity =
$$\left(1 - \left[\frac{\rho_{electrode}}{\rho_{graphite}}\right]\right) * 100$$

where $\rho_{electrode}$ and $\rho_{graphite}$ are the densities of the composite electrode and the pristine graphite material (e.g., ~2.1 g/cm³ for natural graphite, specified by manufacturer), respectively. The density of the composite electrode, $\rho_{electrode}$, was obtained by measuring the mass of an electrode and dividing by its overall volume.

Text S2. Calculation of the theoretical interlayer surface area & comparison to measured external surface area:

Calculation of theoretical surface area of one side of a graphene layer¹:

The unit cell of graphene is a two-dimensional rhombus that contains two carbon atoms and has an area of 0.052 nm². The mass of each unit cell is equal to the mass of two carbon atoms:

Mass of graphene unit cell =
$$2 * 12.011 \text{ amu} * \frac{1.6605*10^{-24} \text{ g}}{1 \text{ amu}} = 3.99 * 10^{-23} \text{ g}$$

Thus, the theoretical specific surface area of one side of a graphene layer is:

Theoretical specific surface area (one - side) =
$$\frac{A}{M} = \frac{0.052 \text{ } nm^2}{3.99*10^{-23} g} = 1.31*10^{21} \frac{nm^2}{g} = 1315 \frac{m^2}{g}$$

Comparison of theoretical interlayer and measured "external" surface areas:

Accounting for the typical porosity (~40%) of a graphite electrode, the theoretical interlayer specific surface area is:

Theoretical specific surface area (one – side, porous) =
$$(1-0.4)\left(1315\frac{m^2}{g}\right) = 789\frac{m^2}{g}$$

The measured BET specific surface area of synthetic graphite (highest among the electrodes studied here) was $9.3 \, \mathrm{m}^2/\mathrm{g}$. Thus, for synthetic graphite, the measured BET surface area is $\sim 1.2\%$ of the total graphene interlayer surface area (one-sided basis). The measured BET surface area for natural and pyrolytic graphites is 0.7% and 0.1% of the graphene interlayer surface area, respectively. This result establishes that the capacity achieved is dominated by electrochemical intercalation of chloroaluminate anions into the graphite interlayers, as opposed to surface phenomena (e.g., double-layer capacitance or electrochemical reaction of adsorbed species).

Text S3. Calculation of overall composition (C_x[AlCl₄]) of a fully-intercalated graphite electrode:

The average composition of an intercalated graphite electrode can be calculated from the discharge capacity per mass of graphite (mAh/g). For NG electrodes, one full discharge yields a capacity of 115 mAh/g, or in terms of number of electrons:

Number of $AlCl_4^-$ anions transferred during one full discharge =

$$\left(\frac{115\,mAh}{g\,graphite}\right)\left(\frac{1\,mol\,e^-}{26800\,mAh}\right)\left(\frac{1\,mol\,AlCl_4^-}{1\,mol\,e^-}\right)\left(\frac{6.022*10^{23}\,molecules\,of\,AlCl_4^-}{1\,mol}\right) = \frac{2.59*10^{21}\,molecules\,of\,AlCl_4^-}{g\,graphite}$$

The above result can be used to calculate the average composition of the intercalated electrode just prior to discharging:

Average composition of NG electrode prior to discharging =

$$\left(\frac{2.59*10^{21}\ molecules\ of\ AlCl_4^-}{g\ graphite}\right)\left(\frac{1.995*10^{-23}g\ graphite}{1\ atom\ of\ C}\right) = \frac{0.0517\ molecules\ of\ AlCl_4^-}{1\ atom\ of\ C} \approx \frac{1\ molecule\ of\ AlCl_4^-}{19\ atoms\ of\ C}$$

Thus, the fully intercalated NG electrode has 1 AlCl₄ anions for every 19 C atoms, yielding an average composition of $C_{19}[AlCl_4]$. This result is similar to a comparable NG system studied by Elia *et al.*², who computed $C_{20}[AlCl_4]$. Performing the same calculation for SG and PG yields average compositions of $C_{28}[AlCl_4]$ and $C_{34}[AlCl_4]$, respectively.

The experimental capacity of the first charge of the natural graphite electrode is 160 mAh/g, which is higher than the discharge capacity of 115 mAh/g, likely due to a combination of irreversible electrochemical side reactions (e.g., electrolyte degradation) and intercalated $AlCl_4^-$ ions that become "trapped", i.e., unable to de-intercalate. It is informative to compute the average composition of the fully-charged NG electrode assuming that the additional 45 mAh/g observed on the first charge is due solely to trapped ions, which yields $C_{14}[AlCl_4]$. The actual average composition of the fully-charged natural graphite is thus somewhere between $C_{19}[AlCl_4]$ (neglecting ion trapping) and $C_{14}[AlCl_4]$.

Text S4. Estimation of theoretical capacity & ion stage numbers via Coulombic & geometric arguments.

Calculation of interlayer packing density and theoretical capacity of stage-1-intercalated graphite using hard-sphere model:

We first estimate the theoretical capacity of stage-1-intercalated graphite assuming the AlCl₄ ions to be rigid, non-interacting spheres (ionic diameter = 5.28 Å)³ and maximum 2D hexagonal packing of circles (packing fraction of 0.907). The ratio of the cross-sectional area of AlCl₄ anions to the area of the graphene unit cell is:

Ratio of effective area of $AlCl_4^-$ to graphene unit cell =

$$\frac{\textit{Area of AlCl}_4^- / \textit{Fraction of occupied area}}{\textit{Area of graphene unit cell}} = \frac{0.219 \ nm^2 \ / \ 0.907}{0.0524 \ nm^2} = 4.64 \ \frac{\textit{Effective area of AlCl}_4^-}{\textit{Area of graphene unit cell}}$$

Thus, 4.64 graphene unit cells thus comprise the effective area (corrected for packing effects) of 1 $AlCl_4^-$ ion. Since each graphene unit cell has 2 carbon atoms, the maximum $AlCl_4^-$ concentration is $C_{9.3}[AlCl_4]$. Under these assumptions, the theoretical capacity at stage 1 can be computed:

Maximum capacity of stage 1 $AlCl_4^-$ intercalated graphite [hard – sphere model] =

$$\left(\frac{1\ molecule\ of\ AlCl_4^-}{9.3\ atom\ of\ C}\right)\left(\frac{1\ mol\ of\ AlCl_4^-}{1.995*10^{-23}\ g\ graphite}\right)\left(\frac{1\ mol\ of\ AlCl_4^-}{6.022*10^{23}\ molecules\ of\ AlCl_4^-}\right)\left(\frac{1\ mol\ e^-}{1\ mol\ AlCl_4^-}\right)\left(\frac{26800\ mAh}{1\ mol\ e^-}\right) = 240\frac{mAh}{g\ graphite}$$

Estimates of theoretical capacity of stage-1-intercalated graphite using DFT models from literature:

The actual shape, dimensions and packing density of $AlCl_4^-$ ions within the graphite layers will depend strongly upon molecular-level interactions between the $AlCl_4^-$ ions and bounding graphene layers, as well as among the $AlCl_4^-$ ions themselves. Density functional theory (DFT) electronic structure calculations may yield more accurate results. However, the current literature indicates that a range of interlayer packing densities may be stable at different cell voltages. For example, using DFT methods, Gao et al. found that packing 1 $AlCl_4^-$ ion per 2x2 or 3x3 repetition of the graphene unit cell yielded formation energies within 0.01 eV of each other, but that generally, higher interlayer packing densities are more energetically favorable than dilute ones (e.g., compared to 1 $AlCl_4^-$ ion per 4x4 repetition, or even more dilute). Considering only the single graphene layer that hosts the $AlCl_4^-$ ion, the 2x2 and 3x3 configurations correspond to compositions of $C_8[AlCl_4]$ and $C_{18}[AlCl_4]$, respectively, which for stage-1-intercalated graphite would result in theoretical capacities of 279 and 124 mAh/g, respectively. Thus, current DFT methods indicate that high interlayer packing densities are favorable and that a range of interlayer compositions may be possible.

Estimation of average stage number of fully-charged graphite based on a coulometric-geometric model:

The average stage number of the intercalated graphites can be estimated by comparing the average composition $C_x[AlCl_4]$, determined coulometrically from the experimentally measured capacity, to the theoretical composition at a given stage number and interlayer packing density. For example, the natural graphite studied here exhibited a discharge capacity of 115 mAh/g, or an overall composition of $C_{19}[AlCl_4]$ (Text S3). Assuming hard-sphere packing of $AlCl_4$ as a first approximation, stage-2-intercalated graphite would have a theoretical capacity of 120 mAh/g and an average composition of $C_{18.6}[AlCl_4]$. Natural graphite thus exhibits an experimental capacity and composition very close to the theoretical capacity and composition of stage-2-intercalated graphite using the hard-sphere model. Consideration of ion trapping would increase the expected $AlCl_4$ content and thus decrease the average stage number towards stage 1. For example, if all 160 mAh/g of the

first charge of NG were a result of the electrochemical intercalation of $AlCl_4^-$ ions, then the overall composition would be $C_{14}[AlCl_4]$ (Text S3), which would indicate a mixture of stage 1 and stage 2 intercalation based on the hard-sphere packing model. Furthermore, if models using lower interlayer packing densities of $AlCl_4^-$ ions are used, then the graphite would need to exhibit a lower stage number, on average, to hold the same overall concentration of $AlCl_4^-$ ions.

As highlighted in the main text, there are currently discrepancies between the stage numbers of fully-charged graphites determined by XRD methods, Raman spectroscopy, and coulometric-geometric models. Reconciling these discrepancies would provide opportunities to clarify the structure and composition of the chloroaluminate-intercalated graphite electrodes, as well as any role of defects and disorder.

References

- (1) Bonaccorso, F.; Colombo, L.; Yu, G.; Stoller, M.; Tozzini, V.; Ferrari, A. C.; Ruoff, R. S.; Pellegrini, V. Graphene, Related Two-Dimensional Crystals, and Hybrid Systems for Energy Conversion and Storage. *Science* **2015**, *347* (6217), 1246501.
- (2) Elia, G. A.; Kyeremateng, N. A.; Marquardt, K.; Hahn, R. An Aluminum/Graphite Battery with Ultra-High Rate Capability. *Batter. Supercaps* **2018**, *2* (1), 83–90.
- Takahashi, S.; Koura, N.; Kohara, S.; Saboungi, M.-L.; Curtiss, L. A. Technological and Scientific Issues of Room-Temperature Molten Salts. *Plasmas Ions* **1999**, *2* (3–4), 91–105.
- (4) Gao, Y.; Zhu, C.; Chen, Z.; Lu, G. Understanding Ultrafast Rechargeable Aluminum-Ion Battery from First-Principles. *J. Phys. Chem. C* **2017**, *121* (13), 7131–7138.